Depositional Environment of the Paleoproterozoic Yuanjiacun Banded Iron Formation in Shanxi Province, China

Changle Wang,[1,2] Kurt O. Konhauser,[3] and Lianchang Zhang[1,†]

[1] *Key Laboratory of Mineral Resources, Institute of Geology and Geophysics, Chinese Academy of Sciences,*
P.O. Box 9825, Beijing 100029, China

[2] *University of Chinese Academy of Sciences, Beijing 100049, China*

[3] *Department of Earth and Atmospheric Sciences, 1-26 Earth Sciences Building, University of Alberta,*
Edmonton, Alberta, Canada T6G 2E3

Abstract

The Paleoproterozoic (~2.38–2.21 Ga) Yuanjiacun banded iron formation (BIF), located in Shanxi Province, is a Superior-type BIF in the North China craton. This BIF is within a metasedimentary rock succession of the Yuanjiacun Formation, in the lower Lüliang Group, which has undergone lower greenschist-facies metamorphism. Iron oxide (magnetite and hematite), carbonate, and silicate facies are all present within the iron-rich layers. The eastward transition from carbonate- into oxide-facies iron formations is accompanied by a change in mineralogical composition from siderite in the west through magnetite-ankerite and magnetite-stilpnomelane assemblages in the transition zone to magnetite and then hematite in the east. These distinct lateral facies are also observed vertically within the BIF, i.e., the iron mineral assemblage changes upsection from siderite through magnetite into hematite-rich iron formation. The oxide-facies BIF formed near shore, whereas carbonate (siderite)- and silicate-facies assemblages formed in deeper waters. Based on detailed analyses of these variations on a basinal scale, the BIF precipitated during a transgressive event within an environment that ranged from deep waters below storm wave base to relatively shallow waters. The BIF samples display distinctively seawater-like REEs + Y profiles that are characterized by positive La and Y anomalies and HREEs enrichment relative to LREEs in Post-Archean Australian shale-normalized diagrams. Consistently positive Eu anomalies are also observed, which are typical of reduced, high-temperature hydrothermal fluids. In addition, slightly negative to positive Ce anomalies, and a large range in ratios of light to heavy REEs, are present in the oxide-facies BIF. These characteristics, in combination with consistently positive $\delta^{56}Fe$ values, suggest that deposition of the BIF took place along the chemocline where upwelling of deep, anoxic, iron- and silica-rich hydrothermal fluids mixed with shallower and slightly oxygenated seawater. The ankerite displays highly depleted $\delta^{13}C$ values and the carbonate-rich BIF has a high content of organic carbon, suggesting dissimilatory Fe(III) reduction of a ferric oxyhydroxide precursor during burial of biomass deposited from the water column; that same biomass was likely tied to the original oxidation of dissolved Fe(II). The fact that the more ferric BIF facies formed in shallower waters suggests that river-sourced nutrients would have been minimal, thus limiting primary productivity in the shallow waters and minimizing the organic carbon source necessary for reducing the hematite via dissimilatory Fe(III) reduction. By contrast, in deeper waters more proximal to the hydrothermal vents, nutrients were abundant, and high biomass productivity was coupled to increased carbon burial, leading to the deposition of iron-rich carbonates. The deposition of the Yuanjiacun BIF during the onset of the Great Oxidation Event (GOE; ca. 2.4–2.2 Ga) confirms that deep marine waters during this time period were still episodically ferruginous, but that shallow waters were sufficiently oxygenated that Fe(II) oxidation no longer needed to be tied directly to proximal cyanobacterial activity.

Introduction

The North China craton is one of the oldest cratonic blocks in the world, containing rocks as old as ~3.85 Ga (Liu et al., 2008). The North China craton consists of Archean to Paleoproterozoic basement overlain by Mesoproterozoic to Cenozoic cover. Banded iron formations (BIFs) occur extensively throughout the Archean units of the North China craton, and four major iron metallogenic provinces have been recognized: (1) Anshan-Benxi in the northeast, (2) Eastern Hebei in the north, (3) Wutai-Lüliang in the central part, and (4) Xuchang-Wuyang-Huoqiu in the south (Zhai and Santosh, 2013). BIFs within these metallogenic provinces account for more than 60% of iron ore production in China. Many researchers have focused primarily on their geology, geochemistry, and tectonic settings (Zhai and Windley, 1990; Shen et al., 2009; Zhang,

X.J. et al., 2011, Dai et al., 2012; Wan et al., 2012; Zhang, L.C. et al., 2012a). Overall, the BIFs in the North China craton have five distinctive characteristics (1) most are Archean in age, with a peak in the Neoarchean (2.55–2.50 Ga); (2) they commonly occur in successions of supracrustal rocks, mostly in close association with mafic metavolcanic rocks; (3) they have generally undergone amphibolite-facies metamorphism, even up to granulite facies, and display strong deformational features; (4) iron oxide, quartz, and various silicate minerals are dominant in nearly all of the BIFs, accompanied by rare carbonates and sulfides; and (5) they generally formed in association with island arc or back-arc basins (Zhang et al., 2012b).

The Lüliang area is located in the western part of Shanxi Province, where large amounts of banded iron formation are exposed, including the Jianshan, Hugushan, and Yuanjiacun BIFs. Previous work (Shen et al., 1982; Tian et al., 1986; Zhu and Zhang, 1987; Shen, 1998; Wang et al., 2014, 2015) on

geologic aspects suggested that the BIFs are Superior type (e.g., Gross, 1980; see also Bekker et al., 2012) because they are laterally extensive and closely associated with clastic sedimentary rocks, and likely formed on passive margins. In addition, based on detailed geochronological studies of the overlying metavolcanic rocks and interbedded clastic metasedimentary rocks (Liu et al., 2012; Lui et al., 2014; Wang et al., 2015), the depositional age of the Yuanjiacun BIF can be constrained to ~2.38 to 2.21 Ga, which contrasts with the general paucity of giant BIF deposition worldwide during the time interval of 2.4 to 2.0 Ga (Isley and Abbott, 1999; Bekker et al., 2010). Therefore, this terrane offers the possibility to directly study the geochemical characteristics of BIF that formed during the pronounced rise of atmospheric oxygen between 2.4 to 2.2 Ga (Bekker et al., 2004; Hannah et al., 2004; Konhauser et al., 2011a).

Despite previous studies of the Yuanjiacun BIF that focused on the source of the iron (Li et al., 2010; Hou et al., 2014; Wang et al., 2014), limited information is available on the paragenetic sequence and depositional environment. In this regard, we present the first comprehensive set of field and petrologic data, together with detailed geochemical analyses, of the Yuanjiacun BIF.

Geologic Background

The basement of the North China craton can be divided into the eastern and western blocks and the intervening Trans-North China orogen (Zhao et al., 2005). Basement rocks of the orogen consist of Neoarchean to Paleoproterozoic tonalite-trondhjemite-granite (TTG) gneisses, supracrustal rocks (metamorphosed sedimentary and volcanic rocks), syn- to post-tectonic granites, and mafic dikes (Liu et al., 2011; Zhao and Zhai, 2013). The Lüliang Complex is situated in the western portion of the Trans-North China orogen, where large amounts of Paleoproterozoic supracrustal rocks and granitoid intrusions are exposed. These supracrustal rock sequences can be divided into four main groups, consisting of, from bottom to top, the Jiehekou, Lüliang, Yejishan, and Heichashan or Lanhe Groups (Fig. 1). These sequences were intruded by the 2182 to 2151 Ma Guandishan-Chijianling TTG gneiss and the ~1800 Luyashan charnockite (Zhao et al., 2008).

The Lüliang Group is found only in the Jinzhouyu area and is more than 15,000 m thick (Yao, 1993). It comprises greenschist to amphibolite facies metamorphosed sedimentary and volcanic rocks, with BIF occurring in the lower part of the sequence and metamorphosed volcanic rocks in the upper part (Liu et al., 2012). This sequence is subdivided into four major units, from the base to the top, the Yuanjiacun, Peijiazhuang, Jinzhouyu, and Dujiagou Formations. The Yuanjiacun Formation is a metasedimentary sequence with BIF occurring in the lower succession, which is represented by well-bedded chlorite schist, sericite-chlorite phyllite, sericite schist, quartzite, and minor carbonaceous chlorite schist (Fig. 2A).

Yu et al. (1997) obtained single-grain zircon U-Pb ages of 2051 ± 68 and 2099 ± 41 Ma for mafic metavolcanic rocks in the Jinzhouyu Formation and metarhyolite in the Dujiagou Formation, respectively. In addition, three radiometric ages were reported by Geng et al. (2000, 2008), including zircon U-Pb ages of 2360 ± 95 Ma for interlayered intermediate-felsic volcanic tuff in the Jinzhouyu Formation and 2175 Ma for metarhyolite in the Dujiagou Formation, and a whole-rock Sm-Nd isochron age of 2351 ± 56 Ma for mafic metavolcanic rocks in the Jinzhouyu Formation. Liu et al. (2012) reported an LA-ICP-MS U-Pb zircon age of 2213 ± 47 Ma for a mafic volcanic rock within the Jinzhouyu Formation. Most recently, Liu et al. (2014) obtained the youngest detrital zircon age of ~2205 Ma for metasedimentary rocks in the middle part of the Yuanjiacun Formation, and crystallization ages of 2209 to 2178 Ma for mafic metavolcanic rocks of the Jinzhouyu and Dujiagou Formations. Moreover, Wang et al. (2015) conducted a similar geochronological study on the metasedimentary rocks intercalated with the Yuanjiacun BIF and obtained the youngest zircon age (n = 5) of 2384 ± 45 Ma. Considering that there exists a potential depositional gap characterized by a disconformity between the Peijiazhuang and Jinzhouyu Formations (Tian et al., 1986; Yu et al., 1997), we suggest that the age of the Yuanjiacun Formation is thus constrained to the Paleoproterozoic (~2.38–2.21 Ga).

Geology and stratigraphy of the Yuanjiacun BIF

Exposed strata in the Yuanjiacun area include Paleoproterozoic metamorphosed sedimentary rocks of the Yuanjiacun Formation of the Lüliang Group and Cambrian-Ordovician carbonate strata (Fig. 2A). The Yuanjiacun BIF and associated metasedimentary rocks have undergone lower greenschist-facies metamorphism (Tian et al., 1986; Yu et al., 1997). The BIF is commonly interbedded with chlorite schist, and contacts between them are sharp and well-defined with no sign of grading, erosion, or intermixing. The Yuanjiacun Formation is unconformably overlain by Middle Cambrian limestone (Fig. 3), at the base of which occur two layers of conglomerate-type BIF approximately 2 to 14 m stratigraphically apart. The conglomerate-type BIFs are dominated by poorly sorted, angular pebbles of well-bedded hematite and quartz ranging from 1 cm to several meters with sand-sized carbonate cements. These fluvial-alluvial sediments were derived by the erosion of underlying BIF and were transported over a short distance by rivers and then were deposited in a paleovalley. The Upper Cambrian strata consist of thin limestone and dolomitic limestone.

Based on a regional structural analysis, Tian et al. (1986) proposed a structural model in which a superimposed fold series affected the Yuanjiacun BIF. In general, it plunges south and is part of an inclined structure with dips to the east and reverses to the west. The exposed strata in the north of the study area are in the lower limb of the folds, whereas the upper limb has been eroded. Strata in the south are situated in the upper limb of the folds, whereas the bottom limb is not exposed. Faults that occur in the area are interpreted as post-depositional with little effects on the BIF (Figs. 2A, 3). After determining the structural framework, Shen et al. (1982) and Tian et al. (1986) suggested that strata of the Yuanjiacun area were gradually older from west to east.

Igneous rocks exposed in the study area consist predominantly of metamorphosed diabase dikes and gneissic granite. The former commonly intrude the BIF and associated clastic metasedimentary rocks, with widths varying from several meters to more than 100 m. From north to south, the diabase amount increases, the width becomes larger (Fig. 2A),
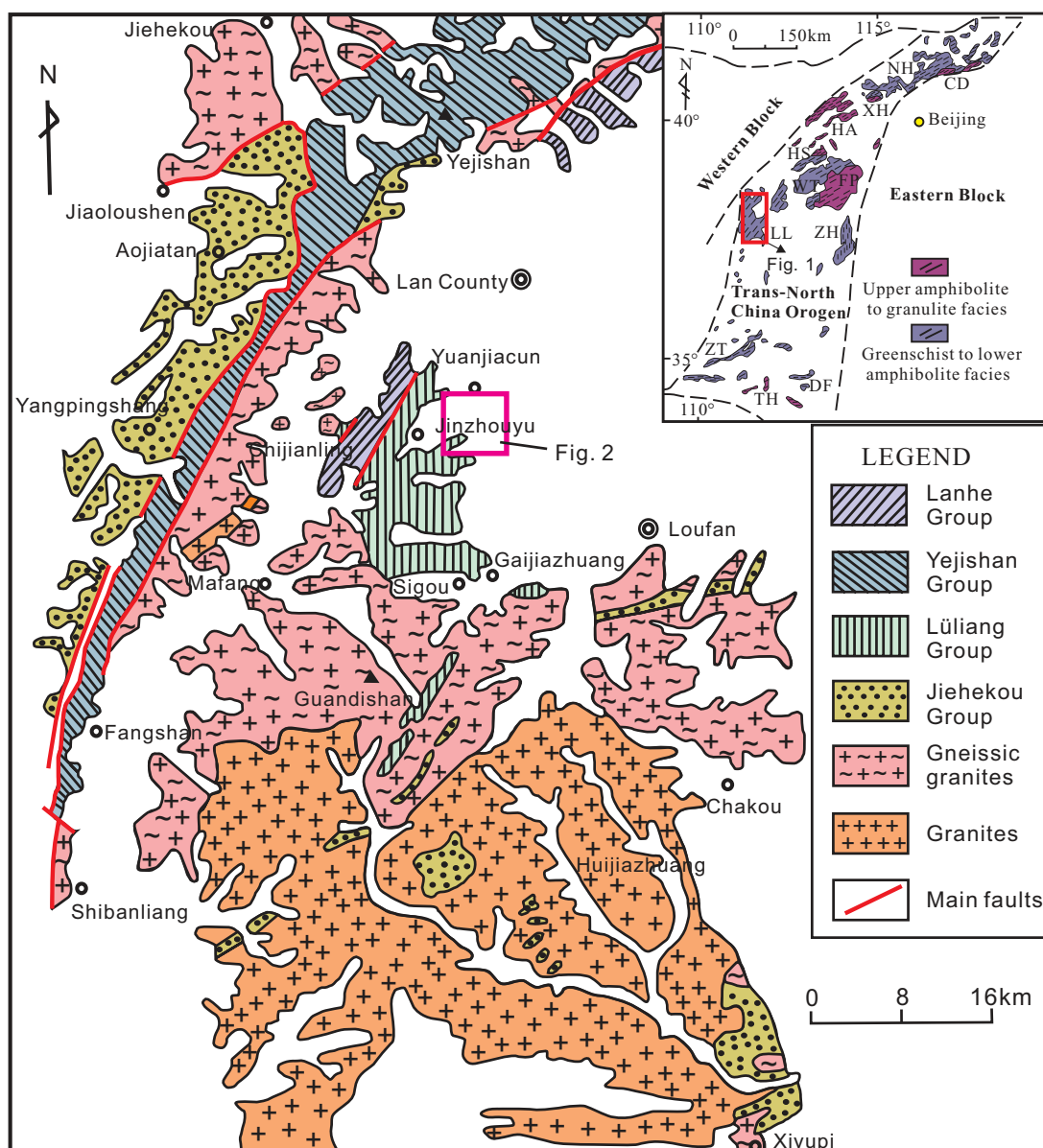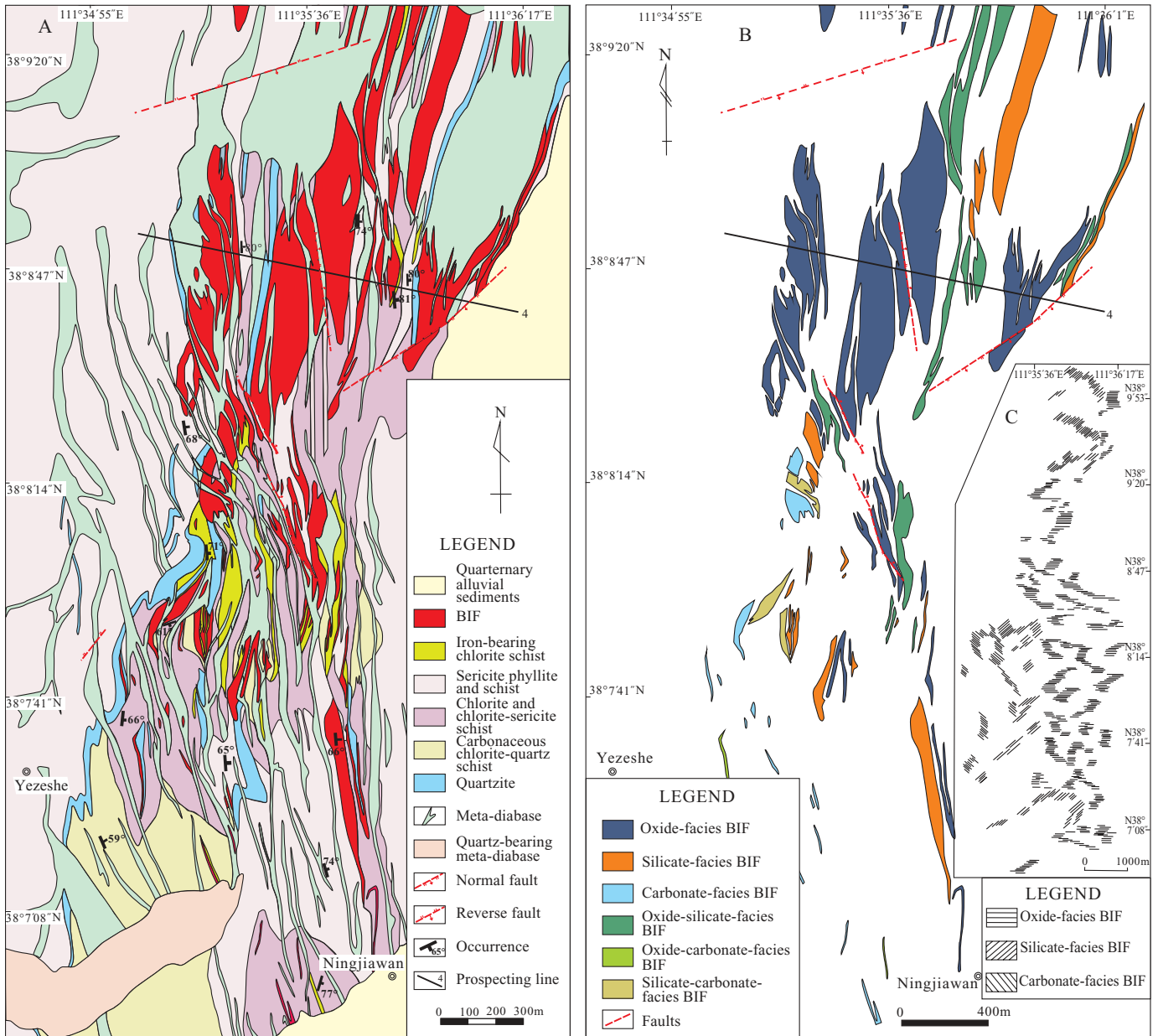
FIG. 1. Geologic sketch of the Paleoproterozoic Lüliang Complex (modified from Wan et al., 2000). Insert map shows location of the Lüliang Complex (LL) in the North China craton (revised after Zhao et al., 2005). Abbreviations: CD = Chengde, DF = Dengfeng, FP = Fuping, HA = Huai'an, HS = Hengshan, LL = Lüliang, NH = Northern Hebei, TH = Taihua, WT = Wutai, XH = Xuanhua, ZH = Zanhuang, ZT = Zhongtiao.

and retrograde metamorphism is enhanced. Located in the northern portion of the Yuanjiacun area, the stocklike gneissic granite intrudes the BIF and has a sharp contact with surrounding rocks. There are no features indicative of alteration or contact metamorphism due to the intrusion of the diabase and granite.

The Yuanjiacun BIF is distributed in a north-northeast–northeast-east orientation, extending 20.5 km in length and 5.8 km in width. Figure 2A and B only depict the middle part of this long belt where the BIF is well developed and exposed. It strikes north-south and north-northeast, dips steeply southeast or east at 70° to 80° (Fig. 3). Individual layers of the BIF vary commonly from less than 1 m to 10s of meters in the section (Fig. 3). Postdepositional deformation is generally

minimal, but with intense folds developed locally. It is noteworthy that some deformation and tight folds are restricted to layers of oxide-facies BIF, and grade upward and downward into adjacent undeformed layers. During subaerial weathering, the outcropping BIF appears to be a predominantly simple, two-component system composed of quartz and iron oxides (e.g., martite; Fig. 3). Additionally, a few quartz or calcite veins cut laminations of the BIF.

Three distinctive sedimentary facies are recognized in the Yuanjiacun BIF on the basis of predominant iron minerals within the iron-rich layers: (1) oxide facies, composed of magnetite and hematite; (2) silicate facies, containing different iron silicate minerals due to varying metamorphic conditions; and (3) carbonate facies, in which the most prominent

FIG. 2. A. Geologic map of the Yuanjiacun BIF, showing distribution of the BIF and associated clastic and chemical metasedimentary rocks (modified from Yao, 1993). B. Geologic sketch showing the distribution of various sedimentary facies of the BIF (modified from Tian et al., 1986). C. Palinspastic map of sedimentary facies in the BIF (modified from Tian et al., 1986). Scope of this map is restricted at both ends (longitude and latitude) by exploration data for prospecting line IV. To highlight the distribution regularity, we merge the transition facies between oxide and silicate facies into oxide facies, and merge the transition facies (oxide- and silicate-carbonate facies) into carbonate facies.

carbonate minerals are siderite and ankerite. As the predominant constituent (>60 vol %) of the Yuanjiacun BIF, the oxide-facies BIF occurs mainly in the north of the study area (Fig. 2B), and is here subdivided into two subfacies: hematite (>24 vol %) and magnetite (>36 vol %) iron formations. The silicate-facies BIF is scattered throughout the region and makes up ca. 30 vol % of the total BIF, whereas the minor carbonate-facies BIF (<10 vol %) is found commonly in the south. In addition to these three main BIF facies, there are transitional facies. Figure 2C, restored based on features of

the regional tectonic framework (Tian et al., 1986), depicts the original distribution of various sedimentary facies in the Yuanjiacun area. The Yuanjiacun BIF is distributed in a north-south direction with an eastward transition from carbonate facies through silicate facies to oxide facies.

Overall, the Yuanjiacun Formation in the study area is a 1.5-km-thick succession of metasedimentary rocks (Shen et al., 1982). Previous detailed field measurement of stratigraphic sections and compilation of drill hole data for several localities have spanned over 20 years (1960–1984). In conjunction
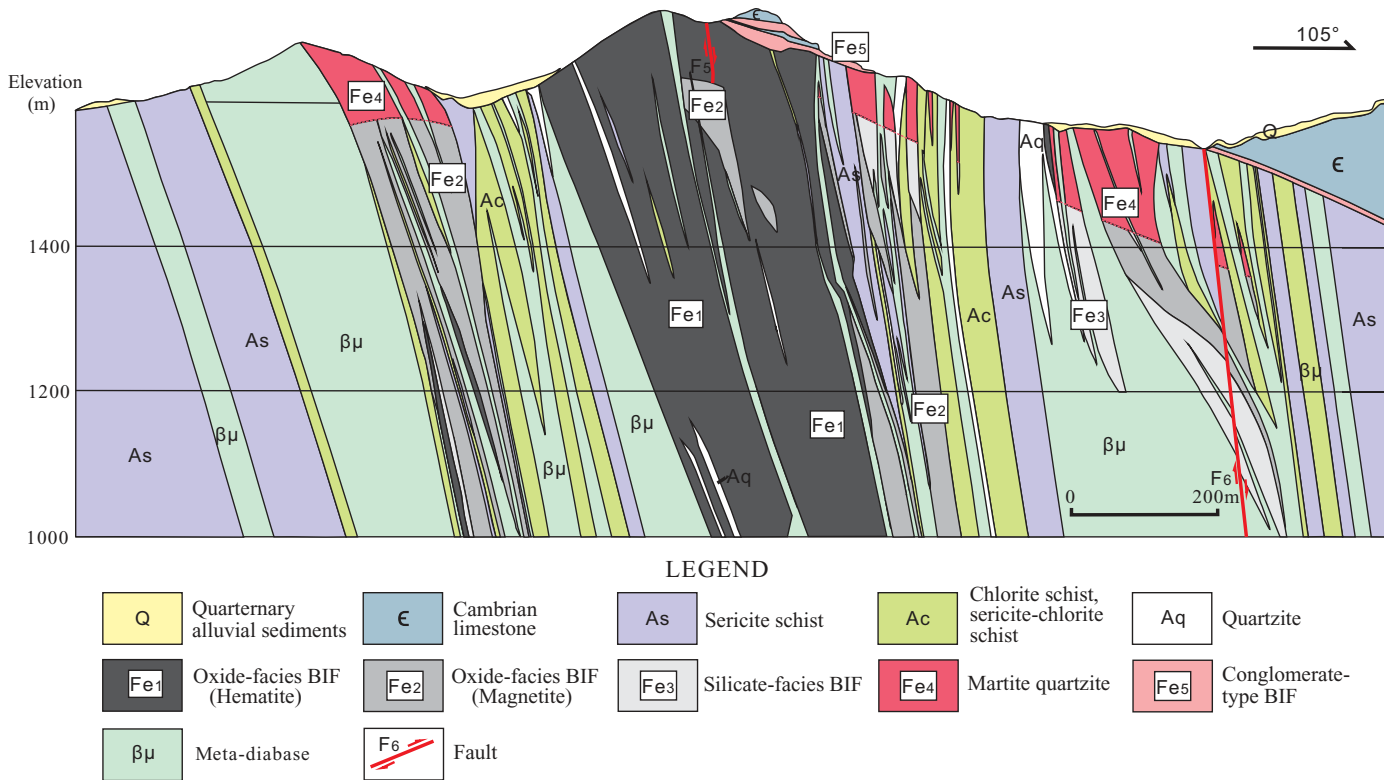
FIG. 3. Cross section of prospecting line IV in the Yuanjiacun area, showing relationship between the Yuanjiacun BIF and associated metasedimentary rocks (modified from Yao, 1993).

with laboratory determinations and analyses and our current investigation, a newly synthesized stratigraphic sequence of the BIF has been constructed. From the base upward, this sequence is divided into three transgressive-regressive cycles (Fig. 4). Within each cycle, the major lithologies commence with coarse- to medium-grained clastic sedimentary rocks, i.e., weakly metamorphosed quartz sandstone or arkose, where ripple marks and trough crossbeddings are well developed, indicating deposition above wave base. Stratigraphically upward, the grain size of these units becomes finer, where the metasedimentary rocks consist mainly of fine-grained metapelite (quartz-sericite phyllite and chlorite schist), which then grade upward into chemical sedimentary rocks represented by iron-bearing quartzite and the BIF with chlorite schist and lesser amounts of interlayered quartz-sericite schist. In particular, the quartz grains of these schists are very small (<0.05 mm) relative to those of metasedimentary rocks in other units (>0.5 mm; Shen et al., 1982). The chlorite schist overlying the BIF underlies an upward-coarsening succession of interlaminated chlorite schist, quartz-sericite phyllite, and sericite schist. A conformable but sharp contact between the BIF and these metasediments is common.

Methods

Detailed petrographic examination using transmitted and reflected light has been carried out to determine the mineralogy and paragenesis of all BIF samples collected from outcrops, drill cores, and exposures in the open pit of the iron mine. Representative samples, including two iron-rich bands (YJC1-3 and YJC4-3), were selected for geochemical

analysis. One to 5 g of rock chips from each sample, without sign of secondary veins or surface weathering, were selected for analyses. Considering that outcrops of unweathered carbonate-facies iron formation are widely scattered, small, and generally difficult to find, little research has been done on this lithology.

Major elements for a set of 22 whole-rock samples of BIF were determined in the Analytical Laboratory at the Beijing Research Institute of Uranium Geology, using a PW2404 X-ray fluorescence spectrometer with an analytical error of less than 5%; the FeO content was obtained by chemical titration. Trace element concentrations were analyzed at the Institute of Geology and Geophysics, Chinese Academy of Sciences in Beijing, using an inductively coupled plasma-mass spectrometer (ICP-MS) Element II Finnigan instrument. Accuracy on the measured concentrations is within ~5 to 10%.

Shale-normalized REE patterns (subscript "SN," normalized to the Post-Archean Australian shale, after McLennan (1989)) are presented for all BIF whole-rock samples. Because the chemical behavior of Y is similar to those of the REEs, Y is inserted between Dy and Ho based on its ionic radius. Thus, Y and the REEs are considered together (Henderson, 1984; Bau and Dulski, 1996, 1999). The La anomaly was calculated using the procedure of Bolhar et al. (2004): $(La/La^*)_{SN} = [La/(3Pr-2Nd)]_{SN}$; the Eu anomaly was calculated as $(Eu/Eu^*)_{SN} = [Eu/(0.67Sm + 0.33Tb)]_{SN}$ (Bau and Dulski, 1996).

Abundances of total organic carbon (TOC) and isotopic compositions of organic carbon ($\delta^{13}C_{org}$) were measured on most samples. Aliquots (200 mg) for TOC analysis were first treated with 10 vol % HCl at 60°C to remove carbonate, and
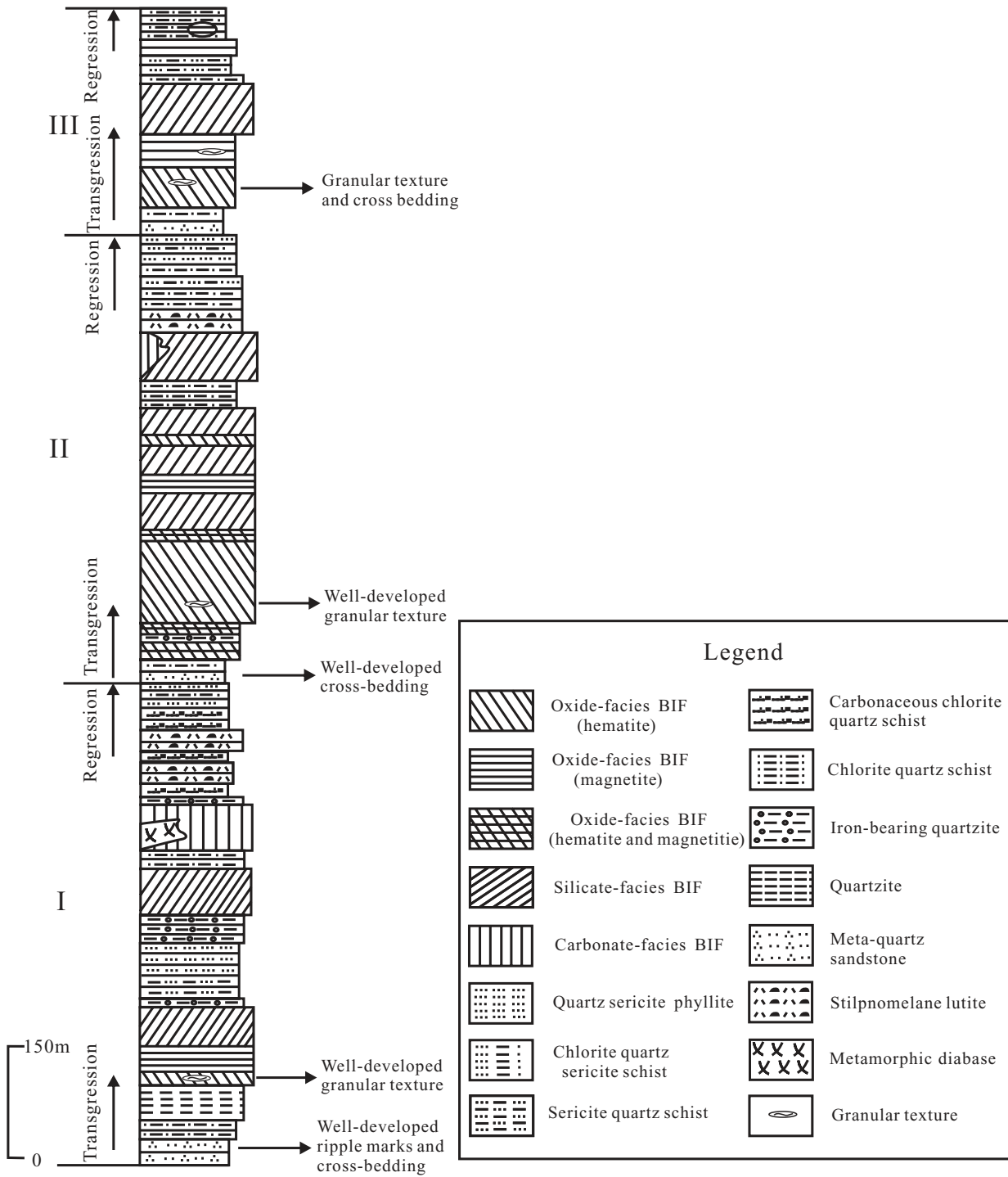
FIG. 4. Stratigraphic column of the Yuanjiacun Formation in the Yuanjiacun area, showing three transgressive and regressive cycles (modified after Shen et al., 1982).

then washed with distilled water to remove HCl. Afterward, the samples were dried overnight (50°C) and then analyzed using an LECO CS-400 analyzer. Sample splits (300 mg–1.5 g) for $\delta^{13}C_{org}$ analysis were acidified with $6N$ HCl in a centrifuge beaker to remove carbonates. The decalcified samples (30–100 mg) + CuO wire (1 g) were added to a quartz tube, and combusted at 500°C for 1 h and 850°C for another 3 h.

Isotopic ratios were analyzed using cryogenically purified CO_2 in a Finnigan MAT-253 mass spectrometer and are reported in standard δ-notation relative to the Vienna Peedee Belemnite (VPDB) standard. Analytical precision for the $\delta^{13}C_{org}$ values is better than ±0.06‰ (1σ).

Carbon and O isotope analyses of ankerite separated from the BIF were performed using the method described in Chen

et al. (2005). Isotopic ratios were determined using a Finnigan MAT 251 mass spectrometer in the stable isotope laboratory at the Institute of Geology and Geophysics, Chinese Academy of Sciences, Beijing. Analytical precision is better than ±0.05‰ (1σ). Carbon and oxygen isotope data are reported using the standard δ-notation, as δ^{13}C and δ^{18}O values, based on the PDB and SMOW scales, respectively.

Iron isotope ratios of magnetite and hematite separated from the oxide-facies BIF were determined with a Thermo-Electron Neptune multicollector ICP-MS following previously published methods (Rouxel et al., 2005) at the ALS Scandinavia Laboratory in Stockholm, Sweden. Iron isotope values are reported relative to the standard IRMM-14 using the conventional δ-notation. The precision for Fe isotope analysis was ±0.08 ‰ (2σ).

Petrography

Oxide-facies BIF

Hematite-rich units: On a microscopic scale, layering in the Yuanjiacun iron formation is diffuse and, in the hematite-rich oxide facies, consists of alternating quartz- and hematite-rich microbands (0.05–7 mm thick). The individual microbands are generally straight and continuous, although deformation is present locally. Contacts between these two types of microbands are commonly sharp (Fig. 5A). Typically, the hematite-rich layers contain a high concentration of small (0.02–0.1 mm) crystals of microplaty hematite that are interconnected to form irregular aggregates intergrown with quartz. The quartz-rich layers are dominated by euhedral to subhedral quartz crystals (0.2 mm), and subordinate fine-grained, dusty hematite (<2 μm). The dusty hematite crystals form individual grains located at the triple point of quartz grains (Fig. 5B), or larger isolated tabular crystals truncating quartz grains (Fig. 5C). In addition, micrometer-sized hematite inclusions occur in places within quartz crystals (Fig. 5B). Specularite (metamorphic recrystallization product of hematite) is present locally, parallel to or truncating the layering.

Some megascopic hematite crystals (granules?; 0.1–1 mm in diam) are observed locally in the BIF, iron-bearing quartzite and/or chlorite schist (Fig. 5D). These crystals occur parallel to the layering or schistosity as defined by chlorite. Tian et al. (1986) and Zhu et al. (1988) recognized oolitic and granular iron oxides (hematite and magnetite), 0.2 to 8 mm in diameter, in some outcrops, including close-packed and lithified mass of ooliths or granules that constitute some iron-rich layers of the BIF. The interstices of these masses are typically filled by chert, but generally with a lower iron content. Crossbedding and graded bedding are present in some of these BIF samples. Overall, such features are similar to those typically found in granular iron formation. It should be also noted that martite (pseudomorphs of magnetite after hematite) commonly forms individual crystals within the hematite-rich microbands. In some cases, martite, together with quartz, constitute microbands that alternate with hematite-rich microbands.

Magnetite-rich units: Textures and sedimentary structures in the magnetite-rich oxide facies are very similar to those in the hematite-rich units. Magnetite microbands alternate with quartz micobands, and in places quartz microbands contain very fine grained, magnetite-rich laminae (Fig. 5E). Magnetite occurs in two forms (1) subhedral grains interconnected to form irregular aggregates, and (2) very fine grained anhedral to subhedral grains intergrown with mosaic quartz in the iron-poor microbands. Euhedral quartz grains are locally truncated by disseminated, coarse-grained magnetite crystals (Fig. 5F). Sedimentary features such as tabular crossbedding (Fig. 5G, I) is rare in the magnetite-rich units. In places, 1- to 2-mm euhedral magnetite crystals are aligned parallel to the layering (Fig. 5H).

Silicate-facies BIF

The mineralogy of the silicate-facies BIF varies both in content and proportion due to the presence of various iron-bearing silicate minerals including stilpnomelane, minnesotaite, chlorite, cummingtonite, and actinolite. Pure magnetite and quartz layers are rare, but locally the quartz layers contain discontinuous laminations composed of fine-grained euhedral magnetite. Large amounts of ankerite occur in the silicate-carbonate- and oxide-carbonate-facies iron formations. It is noteworthy that some chert pods are found in these types of BIF (Fig. 6A), having a flat and lenticular form with internal microbanding. The ends of the pods are not sharply terminated but diffuse into the laminations, as is characteristic of the iron oxide-rich facies. Compared with chert pods in the Hamersley and Kuruman BIFs that have rounded terminations (e.g., Trendall and Blockley, 1970; Beukes and Gutzmer, 2008), the chert pods in the Yuanjiacun BIF pinch out as sharp terminations, which was likely attributed to postdepositional deformation. Ankerite is abundant in compacted silica-rich microbands that occur outside of the pods (Fig. 6B-C).

Stilpnomelane is the most common iron silicate within the BIF. This mineral ranges in length from 0.05 to 0.1 mm and has a width of 0.01 mm and forms thin, continuous laminations (Fig. 6D) or very fine grained sheaves and needles in iron-poor microbands (Fig. 6E). It is closely associated with quartz, magnetite, and ankerite. Detailed examination of quartz microbands reveals the presence of numerous minute and spherical structures or granules (Fig. 7A). The granules are remarkably uniform in size, typically ~0.5 mm in diameter (range 0.4–1.0 mm). They are composed mainly of stilpnomelane, with some quartz and magnetite inclusions, but nearly all have been completely replaced by carbonate minerals and only stilpnomelane relicts are preserved at the edge of these granules (Fig. 7B). The granules are individually surrounded by quartz (Fig. 7A). Similar occurrences have been reported in the Brockman BIF, Western Australia (Rasmussen et al., 2013a); the only difference being that the size of silicate granules in the Yuanjiacun BIF is substantially larger than that of the microgranules (5–20 μm) in the Brockman BIF. They argued that the microgranular texture developed due to clumping of amorphous mud (the precursor mineral of stilpnomelane), forming silt-sized flocules. Those microgranules were resedimented by density currents and deposited in lamina sets as the precursor sediments to the BIF. In our samples, some fine-grained magnetite laminations transect these granules (Fig. 7C), indicating their secondary origin with regards to the granules.

Minnesotaite is generally not as abundant as stilpnomelane. It occurs as fine- to medium-grained needles (0.05–0.2 mm in
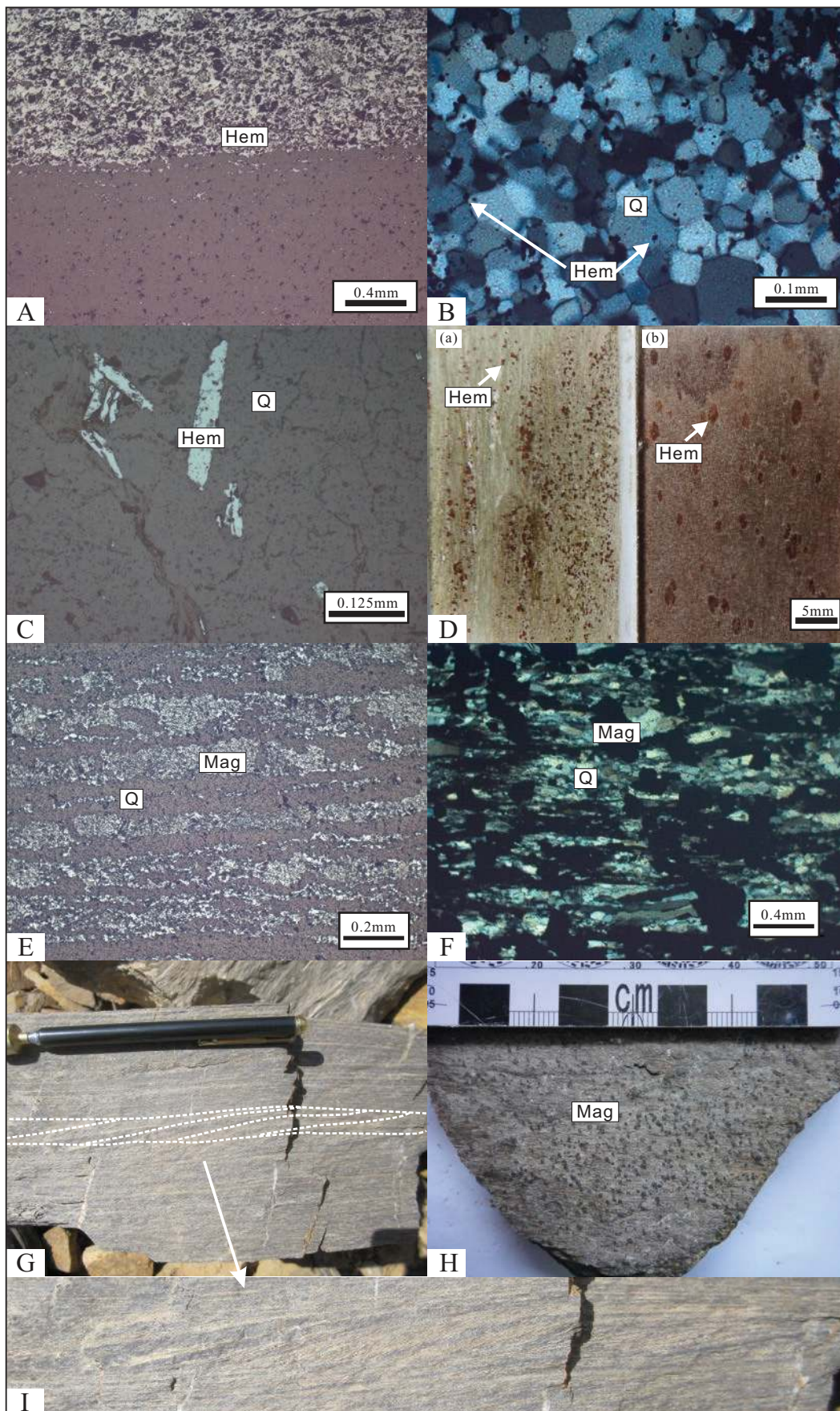
length) scattered within quartz microbands (Fig. 6F), and typically coexists with quartz, magnetite, and stilpnomelane, and locally cuts the fine-grained stilpnomelane sheaves. Chlorite is much more common than minnesotaite, displays a tabular to platy habit, and occurs with magnetite in thin laminations that alternate with quartz microbands that contain lesser amounts of chlorite. Chlorite and relics of stilpnomelane coexist in places (Fig. 6G).

Amphibole is a minor constituent of the silicate-facies BIF and commonly coexists with quartz, magnetite, and calcite. In places, amphibole grains cut stilpnomelane. Cummingtonite occurs as fine-grained sprays and patches (Fig. 7D), as well as fine needles that truncate the layering. Euhedral actinolite grains form clustered arrangements in quartz microbands (Fig. 7E).

Ankerite is present mainly as angular, rhomb-shaped grains (0.05-mm diam) that are evenly distributed in quartz-rich microbands (Fig. 7F). Less common are small ankerite aggregates, which are generally rounded and range from 0.01 to 0.02 mm in diameter (Fig. 7G). The ankerite is locally overgrown by fine-grained magnetite crystals (Fig. 7F) and also contains inclusions of magnetite (Fig. 7H). Veins composed of remobilized ankerite grains in places truncate the microbanding.

Carbonate-facies BIF

The carbonate-facies BIF is only found in the southern part of the Yuanjiacun area. Toward the surface, this lithology changes to limonite and geothite because of strong weathering. As a consequence, fresh outcrops of carbonate-facies BIF are virtually absent, and the only information comes from previous studies (Tian et al., 1986; Zhu et al., 1988). The carbonate-facies BIF is interlayered with carbonaceous chlorite schist and stilpnomelane lutite beds, having a thickness from 5 to 20 m. It typically consists of light to brownish gray quartz microbands that alternate between darker brownish-gray, carbonate-rich (siderite and ankerite) microbands. Iron oxide minerals are generally absent, but organic matter and pyrite are common trace constituents. The siderite crystals form as subhedral rhomboids, locally showing the development of weathered rims.

Geochemistry

Major element composition

The major oxide components in the Yuanjiacun BIF are reported as $Fe_2O_{3(total)}$ (all iron as Fe^{3+}) and SiO_2, which range from 31.84 to 61.58 and 35.66 to 65.36 wt %, respectively (Table 1). Other oxide contents in the oxide-facies BIF, such as Al_2O_3, MgO, and Na_2O, are generally low (<0.2 wt %).

The silicate- and transition-facies BIF have higher contents of MgO (0.21–6.15 wt %) and CaO (0.18–3.39 wt %) than those of the oxide-facies BIF. In addition, CaO concentrations (1.85–3.39 wt %) in the transition-facies BIF, including silicate-carbonate- and oxide-carbonate-facies BIF, are greater due to higher ankerite contents. Examination of the variations in Al_2O_3 reveals that three samples (YJC3-3, YJC4-1, and YJC4-4) have contents of >0.4 wt %, which is attributed to the presence of some Al-rich chlorite; a positive correlation between Al_2O_3 and TiO_2 in these samples suggests the incorporation of siliciclastic material during deposition of the BIF.

Trace and rare earth element compositions

With the exception of some transition metals (e.g., Cr, Ni, and Cu), most trace elements in the Yuanjiacun BIF occur in low concentrations (<20 ppm; Table 1). In terms of incompatible elements, Hf and Th have average concentrations of 0.07 and 0.16 ppm, respectively; whereas, average contents of Sc and Zr are 1.3 and 3.1 ppm, respectively. Low abundances of these elements argue against terrigenous contamination. Within the Al-rich samples, there is a positive correlation between contents of these incompatible elements and Al_2O_3, similarly suggesting the mixing of clastic material with iron-rich chemical precipitates.

The Yuanjiacun BIF is characterized by low ΣREE + Y, ranging from 1.34 to 33.2 ppm (Table 1). Post-Archean Australian shale-normalized REE + Y patterns are presented in Figure 8A-D, in which the BIFs are grouped according to different sedimentary facies. All samples display similar patterns with HREE $((La/Yb)_{SN} <1)$ and MREE $((Sm/Yb)_{SN} <1)$ enrichments relative to LREE, excluding the three samples (YJC3-3, YJC4-1, and YJC4-4) that are slightly enriched in LREE. They also show consistently positive La, Eu, and Y anomalies, except for sample YJC4-4, which lacks positive La anomalies. In addition, in samples of the hematite-rich oxide facies there is major variability in light to heavy REE ratios $((La/Yb)_{SN} 0.16–0.74)$ compared to those of the other BIF facies. Large positive Eu anomalies $((Eu/Eu^*)_{SN} 1.47–3.51)$ are observed in the carbonate-rich transition facies.

The discrimination and identification of Ce anomalies is complicated by possibly anomalous abundances of La. Bau and Dulski (1996) established a discrimination diagram, based on combined $(Ce/Ce^*)_{SN}$ and $(Pr/Pr^*)_{SN}$ values, to distinguish "real" from "false" anomalies of Ce within BIF. In Figure 9, plots for late Paleoproterozoic (2.0–1.8 Ga; field A) and Archean/early Paleoproterozoic (>2.4 Ga) BIFs (field B; Planavsky et al., 2010; Zhang et al., 2011; Dai et al., 2012), as well as previous studies on REE systematics of the magnetite-rich oxide facies

FIG. 5. Photomicrographs and field photos, showing representative textures and petrographic relationships among main mineral phases in the oxide-facies BIF. A. Quartz-rich microbands with scattered crystals of dusty hematite (Hem; 2 μm in size) and contact between the quartz- and iron-rich microbands that are commonly sharp (reflected light). B. Small hematite grains found either within or located at triple junctions of quartz (Q) crystals (crossed polarizers). C. Quartz-rich microband with microplaty hematite crystals cutting quartz grains (reflected light). D. Photographs of chlorite schist in two thin sections, showing hematite granules (?) occurring parallel to schistosity defined by chlorite. E. Magnetite (Mag) crystals forming either irregular aggregates in iron-rich microbands or small dispersed grains in quartz-rich microbands (reflected light). F. Large euhedral and isolated magnetite crystals truncating the banding (crossed polarizers). G. Tabular crossbedding within the BIF (enhanced with white-dashed lines) with small dip angles; pen is 15.5 cm long. H. Macroscopic magnetite crystals (1–2 mm in size) occurring parallel to banding. I. Close-up view of crossbedding shown in (G).
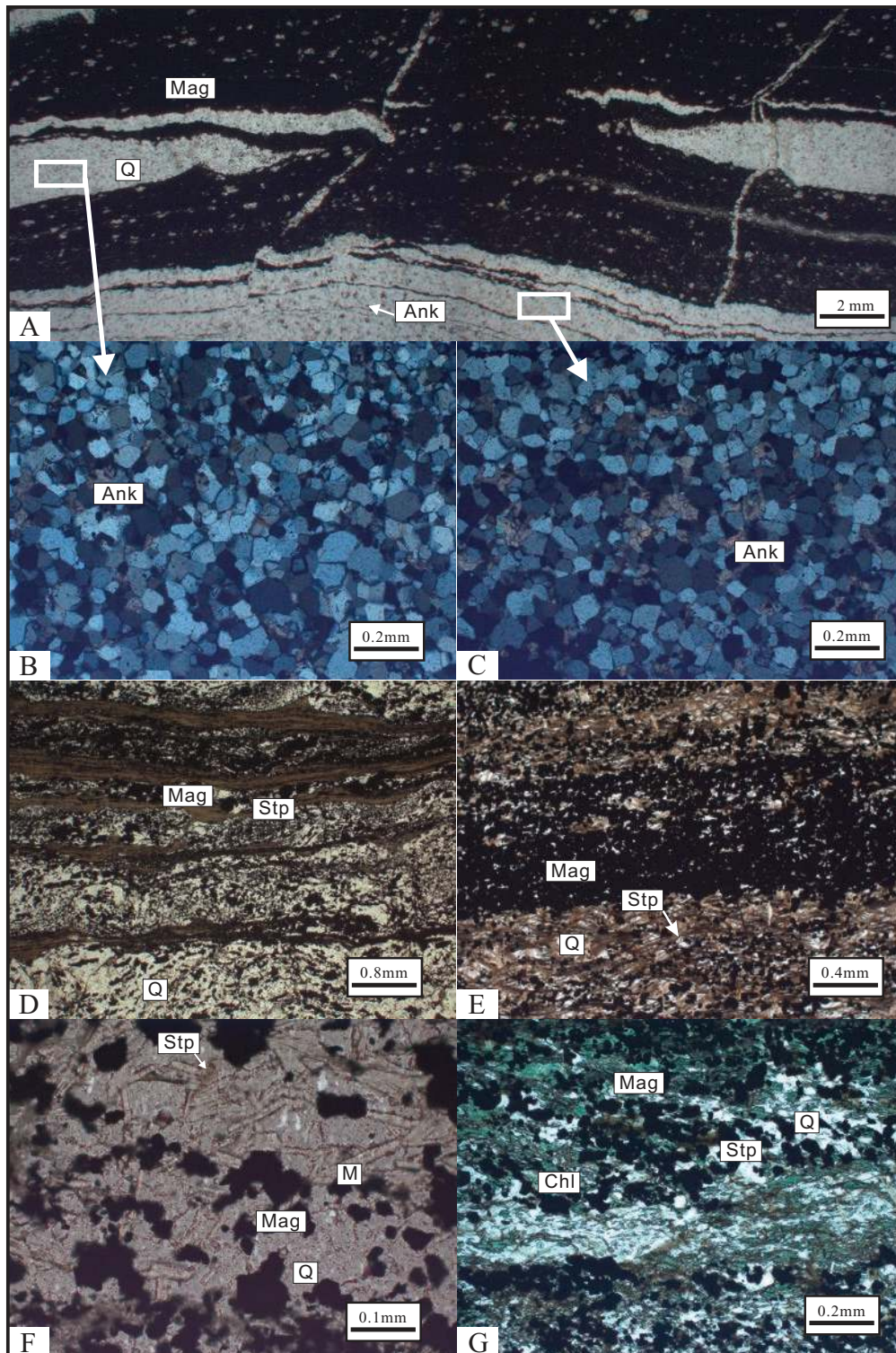
FIG. 6. Photomicrographs showing typical textures of chert pods in the BIF. A. Discontinuous chert pods in iron-rich mesobands containing finely laminated magnetite (Mag; plane-polarized light). Ank = ankerite, Q = quartz. B. Very small amount of ankerite occurs within the chert pods (crossed polarizers). C. Large numbers of ankerite grains occur in quartz-rich microbands outside of chert pods (crossed polarizers). D-G. Photomicrographs under plane-polarized light showing representative textures of stilpnomelane (Stp), ferro-talc-minnesotaite (M), and chlorite (Chl) in the silicate-facies iron formation. D. Stilpnomelane microbands truncating quartz and magnetite microbands. E. Stilpnomelane bundles intergrown with quartz and magnetite, occurring along edges of subhedral quartz crystals. F. Minnesotaite intergrown with magnetite and quartz in quartz bands, and tabular stilpnomelane replaced by minnesotaite. G. Chlorite intergrown with magnetite and quartz, occurring either as microbands comprising mainly magnetite and stilpnomelane or scattered anhedral crystals in quartz bands; note tabular stilpnomelane is locally replaced by chlorite.
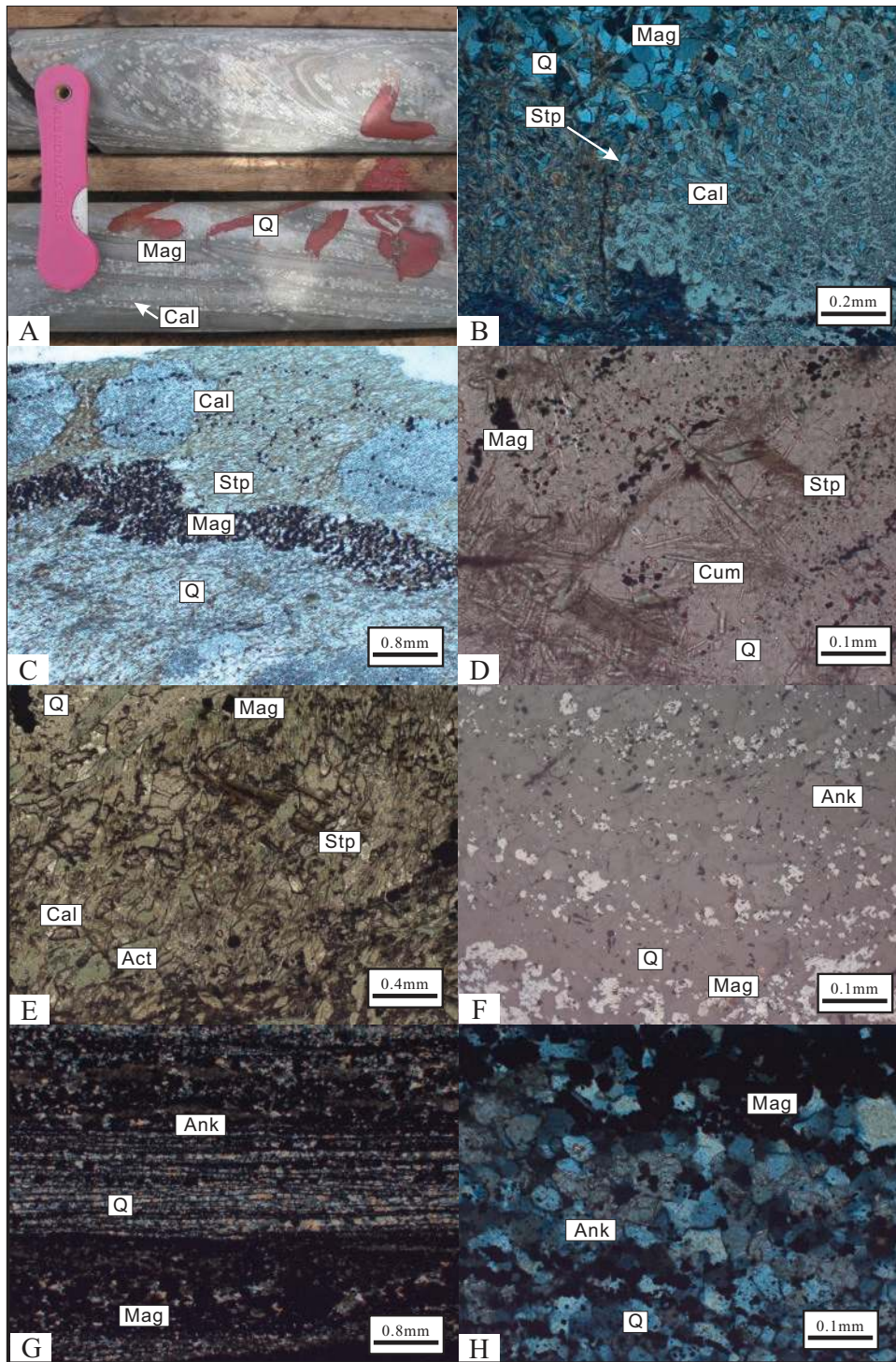
FIG. 7. Photomicrographs and field photos of stilpnomelane (Stp) granules found locally in quartz-rich microbands; nearly all stilpnomelane granules are replaced by carbonate. A. Calcite (Cal) grains of relatively uniform size, typically ~1-mm diam, along edges of quartz microbands. Mag = magnetite, Q = quartz. B. Relicts of stilpnomelane preserved at edges of calcite grains, and stilpnomelane granules containing quartz and magnetite inclusions (crossed polarizers); note tabular stilpnomelane is replaced by carbonate. C. Finely laminated magnetite penetrating stilpnomelane granules (plane-polarized light). Photomicrographs showing representative textures of cummingtonite (Cum), actinolite (Act), and ankerite (Ank) in the silicate-facies iron formation. D. Cummingtonite bundles intergrown with magnetite and quartz, and replacing early stilpnomelane (plane-polarized light). E. Cummingtonite bundles truncating the banding (crossed polarizers). F. Euhedral actinolite intergrown with magnetite, quartz, and calcite, and replacing early stilpnomelane (plane-polarized light). G. Subhedral ankerite evenly distributed in quartz microbands; subhedral-euhedral magnetite crystals occur along edges of ankerite (reflected light). H. Microbands comprising anhedral aggregates of anhedral ankerite and magnetite alternating with quartz microbands (crossed polarizers). I. Ankerite forming euhedral rhomboids with edges commonly displaying corrosion and containing magnetite inclusions (crossed polarizers).

TABLE 1. Major Elements (wt %) and Selected Trace Elements (ppm) of the Yuanjiacun BIF

Sample no.	YJC1-1	YJC1-2	YJC1-3	YJC1-4	YJC1-5	YJC1-6	YJC1-7	YJC1-8	YJC1-9	YJC2-1	YJC2-2	YJC2-3
Facies	Oxide facies (hematite)									Oxide facies (magnetite)		
SiO_2	48.87	55.75	37.95	48.71	52.04	56.62	48.40	50.00	53.50	65.36	53.34	51.88
Al_2O_3	0.15	0.07	0.07	0.02	0.06	0.05	0.15	0.07	0.03	0.08	0.05	0.05
$Fe_2O_{3(total)}$	50.49	43.77	61.58	50.94	47.50	42.45	50.63	49.60	46.19	31.84	45.83	47.52
MgO	0.09	0.10	0.11	0.07	0.09	0.12	0.05	0.02	0.02	0.19	0.18	0.11
CaO	0.07	0.07	0.04	0.05	0.05	0.34	0.22	0.11	0.06	1.07	0.20	0.09
Na_2O	0.01	0.01	0.02	0.06	0.04	0.06	0.01	0.01	0.01	0.01	0.03	0.02
K_2O	0.01	0.01	0.01	0.01	0.01	0.01	0.01	0.00	0.00	0.01	0.01	0.01
MnO	0.01	0.01	0.01	0.01	0.01	0.01	0.00	0.01	0.01	0.03	0.01	0.01
TiO_2	0.01	0.01	0.01	0.01	0.01	0.01	0.01	0.01	0.01	0.01	0.01	0.01
P_2O_5	0.03	0.01	0.01	0.02	0.01	0.03	0.01	0.04	0.02	0.04	0.11	0.06
LOI	0.29	0.13	0.10	0.02	0.09	0.31	0.44	0.07	0.07	1.37	0.16	0.26
Total	100.02	99.93	99.91	99.91	99.90	100.01	99.93	99.93	99.92	100.00	99.91	100.01
FeO	0.54	0.63	0.62	0.58	0.66	0.59	0.76	0.65	0.98	3.25	3.80	3.96
Li	1.19	0.50	0.65	0.44	0.53	0.57	1.25	1.07	0.62	1.11	0.87	0.53
Be	0.20	0.17	0.19	0.23	0.25	0.29	0.27	0.60	0.40	0.18	0.16	0.16
Sc	0.62	0.74	0.58	0.44	0.49	2.04	0.31	2.63	2.32	0.88	0.67	0.75
V	19.90	9.24	8.24	5.96	7.43	13.26	6.86	6.54	8.08	2.93	4.23	5.68
Cr	182.55	384.20	350.04	271.72	327.76	341.85	353.34	348.61	571.36	242.69	228.70	233.70
Co	22.92	6.39	6.39	2.28	3.14	8.10	6.12	4.75	5.41	3.89	4.12	2.68
Ni	13.85	13.94	12.24	9.52	9.98	10.89	13.36	12.53	19.40	11.38	17.87	17.68
Cu	2.00	2.23	2.09	4.10	5.12	12.19	9.99	13.63	8.27	18.41	9.60	4.13
Zn	2.62	1.17	0.98	0.84	0.82	1.97	2.78	1.74	1.78	0.91	0.50	0.84
Ga	1.22	0.72	0.74	0.05	0.13	0.57	0.51	0.94	1.02	0.26	0.28	0.23
Rb	0.92	0.84	0.88	1.35	0.93	0.43	0.95	0.54	0.56	0.11	2.14	8.56
Sr	5.33	3.62	2.52	3.15	3.07	3.29	2.92	5.23	4.03	4.08	3.09	2.89
Zr	2.48	1.59	1.49	0.38	0.57	1.54	1.64	5.34	5.37	0.39	0.56	0.36
Nb	2.08	0.50	0.49	0.07	0.10	0.57	0.25	0.19	0.22	0.08	0.11	0.11
Cs	0.03	0.03	0.06	0.05	0.06	0.03	0.10	0.02	0.01	0.17	0.03	0.02
Ba	3.30	2.65	2.29	3.06	5.69	0.80	4.73	3.40	2.12	2.29	2.67	2.40
La	2.74	1.46	0.93	0.10	0.11	2.06	4.86	2.00	1.31	0.28	0.75	0.65
Ce	4.62	1.90	1.22	0.18	0.15	3.88	7.30	3.36	2.12	0.54	0.94	0.81
Pr	0.70	0.27	0.16	0.03	0.03	0.63	0.86	0.43	0.27	0.10	0.16	0.16
Nd	2.87	1.06	0.55	0.13	0.14	3.05	3.17	1.89	1.26	0.53	0.77	0.90
Sm	0.59	0.23	0.10	0.05	0.05	0.71	0.68	0.47	0.36	0.13	0.13	0.20
Eu	0.19	0.09	0.04	0.03	0.03	0.36	0.30	0.30	0.26	0.07	0.06	0.08
Gd	0.66	0.35	0.12	0.06	0.07	0.98	0.96	0.56	0.52	0.16	0.17	0.32
Tb	0.11	0.07	0.02	0.01	0.01	0.16	0.18	0.09	0.10	0.03	0.03	0.05
Dy	0.71	0.42	0.12	0.07	0.08	1.03	1.18	0.60	0.70	0.15	0.17	0.34
Y	4.53	2.72	1.00	0.55	0.57	8.25	9.67	4.33	5.82	1.10	1.45	2.88
Ho	0.17	0.11	0.03	0.02	0.02	0.24	0.28	0.13	0.17	0.03	0.04	0.08
Er	0.51	0.31	0.08	0.05	0.05	0.70	0.71	0.37	0.48	0.09	0.13	0.23
Tm	0.07	0.05	0.01	0.01	0.01	0.10	0.09	0.05	0.07	0.01	0.02	0.03
Yb	0.52	0.33	0.09	0.06	0.05	0.69	0.59	0.39	0.49	0.09	0.13	0.22
Lu	0.08	0.05	0.02	0.01	0.01	0.11	0.09	0.06	0.08	0.01	0.02	0.04
Hf	0.04	0.03	0.02	0.00	0.01	0.02	0.04	0.06	0.05	0.01	0.01	0.01
Ta	0.01	0.00	0.00	0.00	0.00	0.00	0.01	0.00	0.01	0.00	0.00	0.00
Pb	0.51	0.21	0.16	0.27	0.28	0.51	0.83	0.67	0.47	0.40	0.29	0.22
Th	0.04	0.02	0.03	0.01	0.01	0.05	0.16	0.04	0.05	0.01	0.02	0.02
U	0.83	0.45	1.15	0.65	0.66	0.71	0.90	2.20	1.93	0.01	0.04	0.08
ΣREE + Y	19.07	9.40	4.51	1.34	1.38	22.94	30.92	15.04	14.02	3.33	4.95	7.00
Y/Ho	27.11	25.90	35.75	28.84	31.67	33.79	34.67	32.82	34.25	33.33	35.24	35.12
Pr/Yb	1.36	0.82	1.75	0.51	0.58	0.90	1.46	1.11	0.56	1.20	1.27	0.71
$(La/Yb)_{SN}$	0.39	0.33	0.74	0.13	0.16	0.22	0.61	0.38	0.20	0.24	0.44	0.21
$(Sm/Yb)_{SN}$	0.57	0.36	0.57	0.48	0.53	0.52	0.58	0.61	0.38	0.79	0.52	0.45
$(La/La^*)_{SN}$	1.04	1.40	1.07	1.23	1.34	1.61	1.20	1.44	1.81	1.98	2.18	21.04
$(Y/Y^*)_{SN}$	1.04	1.03	1.39	1.22	1.21	1.31	1.34	1.23	1.34	1.27	1.38	1.37
$(Pr/Pr^*)_{SN}$	1.11	1.09	1.16	1.05	1.15	1.03	1.05	1.00	0.97	1.04	1.05	0.98
$(Ce/Ce^*)_{SN}$	0.77	0.70	0.72	0.81	0.60	0.78	0.82	0.83	0.82	0.72	0.62	0.59
$(Eu/Eu^*)_{SN}$	1.45	1.43	1.70	2.28	2.23	2.14	1.76	2.91	2.78	2.38	2.18	1.70

TABLE 1. *(Cont.)*

Sample no.	YJC3-1	YJC3-2	YJC3-3	YJC3-4	YJC3-5	YJC4-1	YJC4-2	YJC4-3	YJC4-4	YJC4-5
Facies			Silicate facies				Silicate-carbonate facies			Oxide-carbonate facies
SiO_2	42.74	47.98	49.80	45.63	47.70	44.73	44.66	35.66	55.50	40.30
Al_2O_3	0.02	0.03	2.38	0.05	0.04	0.43	0.11	0.06	1.68	0.15
$Fe_2O_{3(total)}$	52.91	48.17	39.98	53.39	47.23	44.32	50.30	55.75	34.01	54.14
MgO	2.65	2.63	3.69	0.21	3.14	6.15	0.87	1.30	2.41	0.84
CaO	1.07	0.26	0.19	0.18	1.22	2.44	1.85	3.39	2.13	2.37
Na_2O	0.03	0.04	0.06	0.04	0.02	0.04	0.10	0.03	0.08	0.01
K_2O	0.01	0.01	0.33	0.02	0.01	0.18	0.04	0.01	0.52	0.01
MnO	0.05	0.03	0.07	0.01	0.05	0.16	0.05	0.06	0.08	0.05
TiO_2	0.01	0.01	0.11	0.01	0.01	0.02	0.02	0.01	0.04	0.01
P_2O_5	0.13	0.09	0.02	0.09	0.04	0.11	0.07	0.11	0.05	0.11
LOI	0.39	0.68	3.26	0.27	0.42	1.41	1.91	3.59	3.18	1.56
Total	100.01	99.91	99.90	99.90	99.87	99.98	99.97	99.96	99.68	99.55
FeO	16.90	15.38	20.50	8.97	16.65	18.45	12.32	15.20	14.35	15.55
Li	0.26	0.25	0.68	0.61	0.47	0.37	0.21	0.20	1.15	1.47
Be	0.37	0.34	0.56	0.76	1.17	0.48	0.47	0.36	0.57	0.44
Sc	0.18	0.39	3.49	0.46	0.16	0.52	4.90	3.88	2.02	0.40
V	8.59	2.84	23.88	5.90	3.36	4.27	8.05	5.85	17.82	5.78
Cr	258.97	203.65	105.58	260.87	76.06	184.65	175.76	192.92	175.13	219.08
Co	14.43	2.51	3.42	2.60	0.78	2.62	6.39	5.83	3.45	2.95
Ni	11.78	15.27	20.44	8.55	5.45	11.61	11.49	17.18	14.20	8.64
Cu	0.42	0.02	4.70	3.10	2.58	0.37	2.49	2.88	16.88	9.73
Zn	1.84	1.65	14.43	1.98	4.21	13.93	2.17	3.86	6.31	3.58
Ga	0.50	0.23	3.32	0.38	0.28	0.54	1.18	0.69	4.31	0.05
Rb	6.57	0.32	25.33	4.20	1.30	0.05	0.83	1.48	45.43	0.56
Sr	7.57	3.18	22.45	5.16	17.40	15.36	18.04	16.27	50.58	16.21
Zr	0.25	0.30	25.33	0.13	0.30	3.45	1.07	0.85	14.67	0.88
Nb	2.00	0.21	1.67	0.22	0.12	0.17	0.63	0.50	0.76	0.20
Cs	0.08	0.07	4.16	0.59	0.23	1.18	0.89	0.12	8.51	0.12
Ba	3.72	3.03	25.44	2.29	17.78	23.88	3.87	3.37	26.14	3.04
La	0.59	0.54	5.97	0.28	2.18	3.30	0.76	0.56	5.92	3.17
Ce	0.90	0.77	10.75	0.46	3.58	4.56	1.25	0.88	11.28	6.20
Pr	0.14	0.11	1.30	0.10	0.42	0.56	0.18	0.16	1.41	0.95
Nd	0.64	0.53	4.86	0.51	1.89	2.42	0.81	0.80	5.35	4.67
Sm	0.13	0.11	0.80	0.15	0.41	0.36	0.15	0.21	0.99	1.17
Eu	0.09	0.07	0.21	0.10	0.22	0.13	0.12	0.18	0.28	0.55
Gd	0.20	0.17	0.66	0.18	0.52	0.40	0.21	0.29	0.91	1.32
Tb	0.03	0.03	0.09	0.04	0.09	0.06	0.03	0.05	0.13	0.19
Dy	0.23	0.21	0.51	0.23	0.65	0.40	0.25	0.32	0.79	1.12
Y	2.21	1.81	3.15	1.52	5.24	3.24	2.06	2.74	4.94	8.17
Ho	0.06	0.05	0.11	0.06	0.17	0.10	0.07	0.08	0.17	0.26
Er	0.18	0.16	0.34	0.17	0.48	0.29	0.20	0.23	0.46	0.70
Tm	0.03	0.02	0.05	0.02	0.07	0.04	0.03	0.04	0.06	0.09
Yb	0.19	0.16	0.43	0.18	0.47	0.29	0.22	0.26	0.42	0.69
Lu	0.03	0.03	0.08	0.03	0.08	0.05	0.04	0.04	0.07	0.11
Hf	0.01	0.01	0.68	0.00	0.01	0.09	0.02	0.02	0.40	0.02
Ta	0.00	0.00	0.12	0.01	0.00	0.01	0.01	0.00	0.09	0.01
Pb	0.39	0.30	0.92	0.39	2.05	0.45	0.64	0.63	1.25	1.63
Th	0.01	0.01	1.57	0.03	0.05	0.22	0.06	0.02	0.86	0.13
U	0.00	0.01	0.28	0.03	0.02	0.02	0.03	0.03	0.21	0.05
$\Sigma REE + Y$	5.65	4.76	29.30	4.01	16.46	16.20	6.37	6.82	33.19	29.37
Y/Ho	36.83	33.44	27.91	27.62	31.36	32.12	31.66	35.14	28.70	32.04
Pr/Yb	0.75	0.70	3.06	0.55	0.89	1.91	0.84	0.61	3.34	1.39
$(La/Yb)_{SN}$	0.23	0.25	1.04	0.12	0.34	0.83	0.26	0.16	1.04	0.34
$(Sm/Yb)_{SN}$	0.36	0.35	0.95	0.44	0.44	0.62	0.34	0.41	1.20	0.87
$(La/La^*)_{SN}$	1.65	1.85	1.00	2.75	1.77	1.79	1.48	2.30	0.95	1.72
$(Y/Y^*)_{SN}$	1.48	1.36	1.05	1.08	1.27	1.29	1.28	1.38	1.07	1.22
$(Pr/Pr^*)_{SN}$	1.04	1.02	1.06	1.05	0.95	0.99	1.03	1.03	1.07	1.00
$(Ce/Ce^*)_{SN}$	0.72	0.72	0.89	0.64	0.86	0.76	0.78	0.68	0.90	0.82
$(Eu/Eu^*)_{SN}$	2.72	2.45	1.45	2.64	2.34	1.69	3.46	3.51	1.47	2.29

Notes: Total Fe reported as Fe_2O_3; $(Pr/Pr^*)_{SN} = [2Pr/(Ce + Nd)]_{SN}$; $(Ce/Ce^*)_{SN} = [2Ce/(La + Pr)]_{SN}$; $(La/La^*)_{SN} = [La/(3Pr - 2Nd)]_{SN}$; $(Eu/Eu^*)_{SN} = [Eu/(0.67Sm + 0.33Tb)]_{SN}$; $(Y/Y^*)_{SN} = [2Y/(Dy + Ho)]_{SN}$
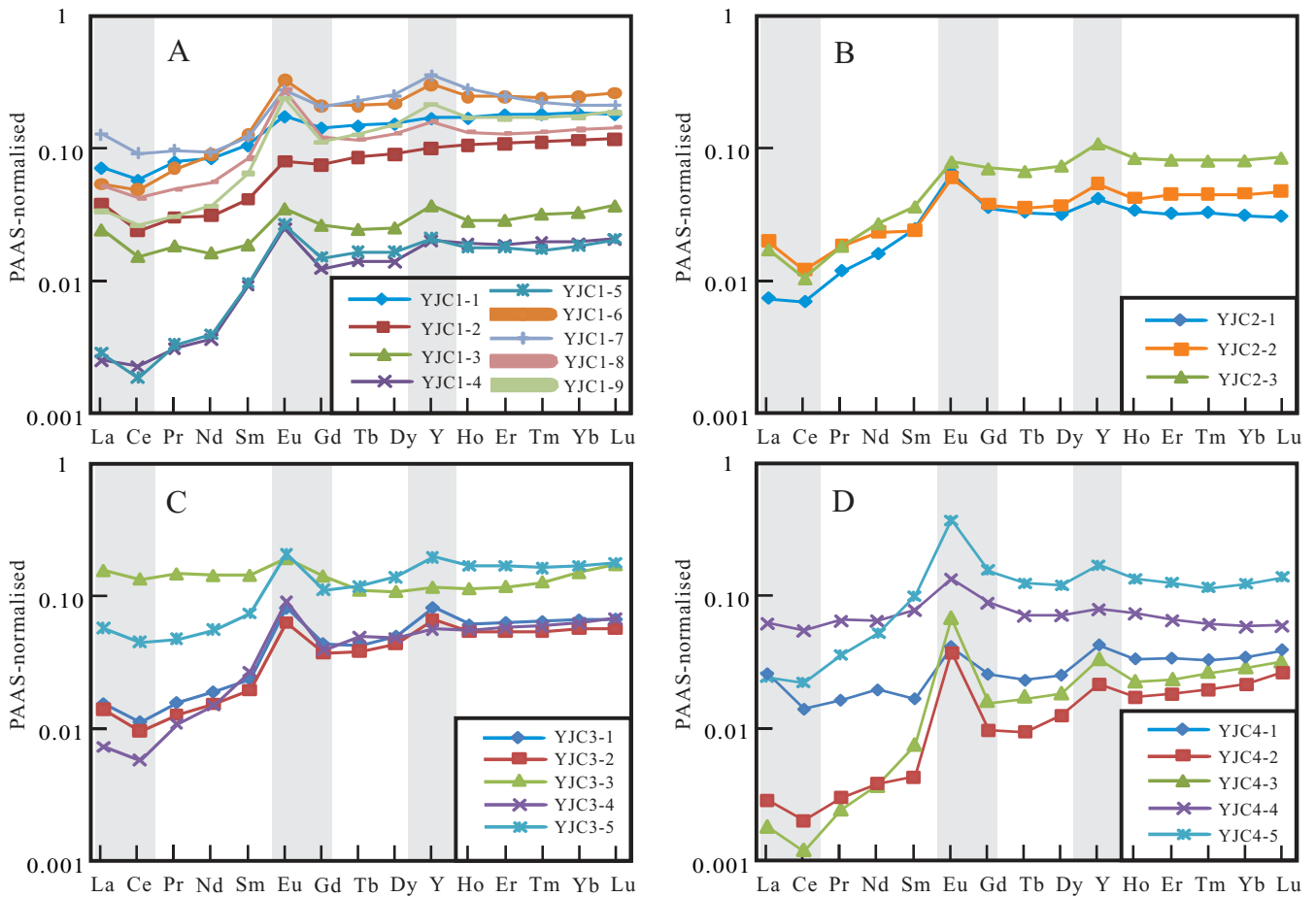
Fig. 8. Post-Archean Australian shale (PAAS)-normalized REE + Y distributions of Yuanjiacun BIF samples. A. Hematite iron formation. B. Magnetite iron formation. C. Silicate-facies iron formation. D. Carbonate-rich facies iron formation. PAAS data from McLennan (1989).
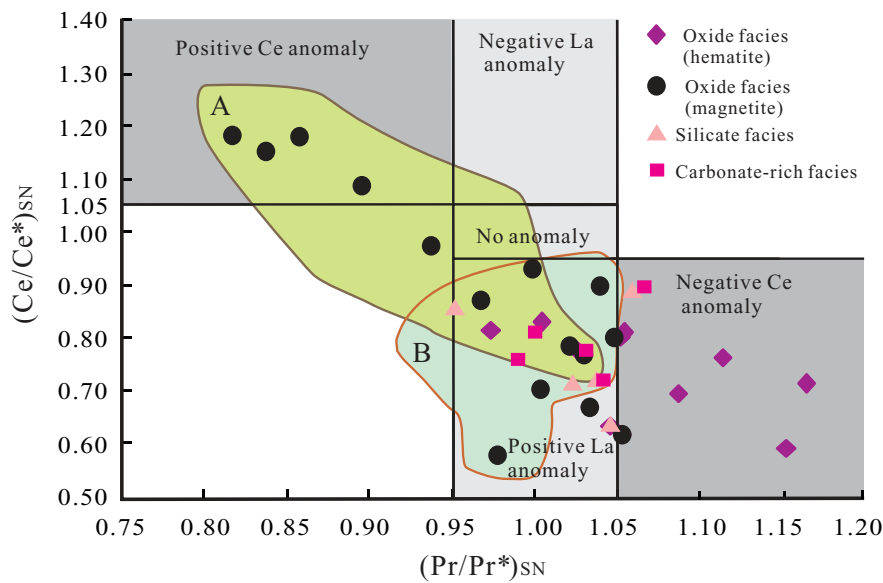

Fig. 9. Plot of Ce and Pr anomalies normalized to PAAS for Yuanjiacun BIF samples, discriminating between positive La anomalies and true Ce anomalies (Bau and Dulski, 1996). Plots of late Paleoproterozoic (<2.0 Ga) (field A; after Planavsky et al., 2010) and Archean and early Paleoproterozoic (>2.4 Ga) (field B; after Planavsky et al., 2010; Zhang et al., 2011; Dai et al., 2012) iron formations, and previous data (after Wang et al., 2014) for the Yuanjiacun magnetite iron formation are also included.

in the Yuanjiacun BIF (Wang et al., 2014), are included. It is evident that the behavior of Ce is complex, showing both positive and negative Ce anomalies for the oxide-facies BIF.

Organic carbon, carbonate carbon, and oxygen isotope compositions

Carbon isotope ratios of organic carbon and contents of total organic carbon (TOC) in the BIF samples are listed in Table 2. TOC ranges from 0.01 to 0.34 wt %, with significantly higher contents in the transition-facies BIF. Carbon isotope ratios of organic matter ($\delta^{13}C_{org}$) are rather uniform, varying from –26.07 to ×19.15‰, with a mean of –23.87‰. There does not appear to be a relationship between TOC and $\delta^{13}C_{org}$. The $\delta^{18}O$ values for the ankerite in the BIF range between 12.67 and 16.72‰; $\delta^{13}C$ values vary from –7.84 to –6.04‰ (Table 3). The range of $\delta^{13}C$ values of the BIF carbonate overlaps those measured for the other iron formations but is more depleted in $\delta^{13}C$ relative to Ca-Mg carbonate rocks (Table 4). In contrast, the $\delta^{18}O$ values of carbonates in the Yuanjiacun BIF are much lower than, for example, those associated with the early Paleoproterozoic Kuruman and Griquatown BIF in South Africa (Table 4).

Iron isotope composition

Iron isotope data for the magnetite- and hematite-rich, oxide-facies BIF are presented in Table 5. Previous data are also included (Hou et al., 2014). Magnetite grains from ten samples yielded $\delta^{56}Fe$ values from 0.35 to 0.89‰, with an average of 0.65‰. Hematite grains from five samples yielded $\delta^{56}Fe$ values varying from 0.40 to 1.09‰, with an average of 0.60‰.

Discussion

Mineral paragenesis and evolution

Petrographic and geochemical data presented here for the Yuanjiacun BIF allow us to establish different generations of mineral formation during diagenesis and metamorphism.

TABLE 2. Total Organic Carbon (TOC) and Carbon Isotope Ratios of Organic Carbon for the Yuanjiacun BIF

| Sample no.	TOC (wt %)	$\delta^{13}C_{org(‰)}$
YJC1-1	0.02	–24.02
YJC1-2	0.02	–24.03
YJC1-3	0.05	NA
YJC1-4	0.04	–25.64
YJC1-7	0.01	NA
YJC2-1	0.06	–19.15
YJC2-2	0.03	–24.44
YJC2-3	0.01	–23.78
YJC2-4	0.04	NA
YJC2-5	0.05	NA
YJC3-1	0.03	–24.17
YJC3-2	0.02	–24.53
YJC3-3	0.06	NA
YJC3-4	0.04	–24.95
YJC3-5	0.04	NA
YJC4-1	0.15	–26.07
YJC4-2	0.27	–23.86
YJC4-3	0.34	–21.81
YJC4-4	0.19	NA
YJC4-5	0.21	NA

Notes: Some samples were not analyzed (NA) for isotope compositions of organic carbon

TABLE 3. Carbon and Oxygen Isotope Composition of Ankerite in the Yuanjiacun BIF

Sample no.	$\delta^{13}C_{PDB}(‰)$	$\delta^{18}O_{SMOW}(‰)$
1	–6.63	13.64
2	–6.32	13.94
3	–6.56	14.13
4	–6.77	13.55
5	–7.24	13.73
6	–6.96	12.67
7	–6.04	15.32
8	–7.58	14.74
9	–7.84	16.67
10	–7.15	16.72

Notes: PDB = Pee Dee Belemnite; SMOW = standard mean ocean water

As in most BIF, microcrystalline quartz is the most abundant mineral. This is not surprising, given that silica concentrations in the Precambrian oceans would have been much higher (~2 mM) than today (~0.1 mM), due to the absence of silica-secreting organisms before the Phanerozoic (Sievier, 1992; Konhauser et al., 2007). Silica precipitation in the Precambrian oceans could have been induced by evaporative- or temperature-induced supersaturation (Garrels, 1987; Posth et al., 2008) or coprecipitation with iron minerals (Ewers, 1983; Konhauser et al., 2007). In the case of the latter, Fischer and Knoll (2009) proposed a model whereby dissolved silica ($Si(OH)_4$) was absorbed onto ferric oxyhydroxides, such as ferrihydrite ($Fe(OH)_3$), to form a siliceous ferric hydroxide precursor that sank to the seafloor, together with organic matter. At the seafloor, oxidation of that organic matter, coupled to dissimilatory Fe(III) reduction, could have liberated some iron, leading to the formation of iron-poor layers (Nealson and Myers, 1990) as follows:

$$CH_3COO^- + 8Fe(OH)_3 \rightarrow 8Fe^{2+} + 2HCO_3^- + 15OH^- + 5H_2O. \quad (1)$$
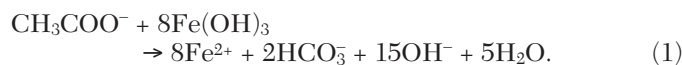
During burial diagenesis, there also may have been vertical escape of silica, which reprecipitated at sediment-water interface, yielding BIF with a higher silica content (Trendall and Blockley, 1970). Alternatively, Krapež et al. (2003) and Pickard et al. (2004) have suggested that all chert in BIF is the siliceous equivalent of modern-day seafloor hardgrounds, in which silica replaced precursor sediment at or below the sediment-water interface. The presence of three-dimensional and microscale lenticularity of chert and relics of precursor sediment within lamina sets and discontinuous bands, as well as erosion surfaces on bedded cherts, show that chert has a replacement origin and formed during early diagenesis, prior to compaction. In either case, high seawater concentrations of silica are needed for incorporation into the original sediment to yield the high SiO_2 observed in the Yuanjiacun BIF.

Hematite displays textural diversity, including anhedral aggregates, and xenomorphic and microplaty grains (Fig. 5A-B). In iron-rich marine environments, the biotic or abiotic oxidation of dissolved Fe(II) leads to the production of Fe(III) oxyhydroxides (Konhauser et al., 2011b). These poorly crystalline Fe phases (e.g., ferrihydrite) can transform into hematite (via dehydration), and goethite and lepidocrocite (through Fe(II)-catalyzed transformation), depending on

TABLE 4. Carbon and Oxygen Isotope Variations in Carbonates from Selected, Essentially Unmetamorphosed Iron Formations

BIF sequence	$\delta^{18}O_{SMOW}$(‰)	$\delta^{13}C_{PDB}$(‰)	Reference
Kuruman and Griquatown Iron Formations, South Africa	19.05~22.25	−8.42~−5.45	Beukes et al. (1990)
Limestone and dolomites at same above location	20.09~26.89	−2.8~−0.1	Beukes et al. (1990)
Kuruman and Griquatown Iron Formations, South Africa	16.1~21.90	−14.8~−7.46	Kaufman (1996)
Kuruman and Griquatown Iron Formations, South Africa	19~21	−12~−2.6	Heimann et al. (2010)
Brockman Iron Formation, Dales Gorge Member, Western Australia	17.6~21	−7.96~−6.92	Kaufman et al. (1990)
Brockman Iron Formation, Dales Gorge Member, Western Australia	NA	−15~−6.5	Craddock and Dauphas (2011)
Wittenoom Dolomite, Hamersley Basin	NA	−1.8~−0.13	Craddock and Dauphas (2011)
Yuanjiacun Iron Formation	12.67~16.72	−7.84~−6.04	This study

Notes: Some samples were not analyzed (NA) for oxygen isotope compositions; PDB = Pee Dee Belemnite, SMOW = standard mean ocean water

pH and solution chemistry (Posth et al., 2014). As previously observed by Schwertmann and Murad (1983), crystallization of ferrihydrite at pH 7-8 is the major pathway for hematite formation. The euhedral hematite crystals in the Yuanjiacun BIF (Fig. 5C) are interpreted as having formed from the low-grade metamorphic crystallization of smaller hematite grains. In general, the preservation of hematite-rich units represents sediment buried in which molar Fe(III)/C_{org} ratios far exceeded the 4/1 molar ratio associated with dissimilatory Fe(III) reduction, because only a small amount of organic carbon, along with sufficient primary Fe(OH)$_3$, was required for the magnetite formation during diagenesis (Konhauser et al., 2005). Consequently, either (1) all of the biomass was oxidized, leaving behind a residue of ferric oxyhydroxide (Konhauser et al., 2005); or (2) there was minimal burial of organic carbon when the precursor ferric oxyhydroxide phases precipitated (Beukes et al., 1990). Based on the low TOC content in the hematite-rich unit, either option is possible.

Two main types of magnetite are found in the Yuanjiacun BIF, namely minute subhedral crystals that form aggregates or massive monomineralic laminae (Fig. 5E), and larger euhedral and isolated crystals that truncate quartz grains (Fig. 5F). The euhedral magnetite is paragenetically late and is regarded as a metamorphic recrystallization product, whereas

TABLE 5. Fe Isotope Data for the Yuanjiacun Oxide-Facies BIF

Sample no.	Mineral	$\delta^{56}Fe$(‰)	$\delta^{57}Fe$(‰)
YJC13-46	Magnetite	0.58 ± 0.03	0.89 ± 0.05
YJC13-49	Magnetite	0.35 ± 0.02	0.54 ± 0.03
YJC13-59	Magnetite	0.84 ± 0.02	1.26 ± 0.03
YJC-04[1]	Magnetite	0.89 ± 0.04	1.30 ± 0.09
YJC-13[1]	Magnetite	0.63 ± 0.10	0.96 ± 0.09
YJC-14[1]	Magnetite	0.76 ± 0.02	1.11 ± 0.13
YJC-20[1]	Magnetite	0.58 ± 0.02	0.86 ± 0.10
YJC-21[1]	Magnetite	0.70 ± 0.02	1.02 ± 0.11
YJC-22[1]	Magnetite	0.68 ± 0.05	1.02 ± 0.09
YJC-23[1]	Magnetite	0.52 ± 0.06	0.80 ± 0.13
YJC1-1	Hematite	0.40 ± 0.03	0.57 ± 0.05
YJC1-3	Hematite	0.41 ± 0.02	0.59 ± 0.03
YJC1-8	Hematite	1.09 ± 0.04	1.59 ± 0.05
YJC1-8r[2]	Hematite	1.09 ± 0.02	1.59 ± 0.03
YJC-12[1]	Hematite	0.41 ± 0.06	0.61 ± 0.07
YJC-24[1]	Hematite	0.72 ± 0.02	1.06 ± 0.06

[1] Data from Hou et al. (2014)
[2] r in sample name denotes a replicate digestion and analysis of the same sample

the aggregates may have formed earlier during diagenesis. In either case, the magnetite is unlikely to represent a primary precipitate. There are at least three plausible mechanisms responsible for the formation of magnetite:

1. Reduction of Fe(III) oxyhydroxide via dissimilatory Fe(III) reduction, which is the generally accepted model based on theoretical, experimental, and petrographic support (Lovley, 1993; Frost et al., 2007; Johnson et al., 2008; Pecoits et al., 2009; Li et al., 2011, 2013). Dissimilatory Fe(III) reduction can produce large Fe isotope fractionations between Fe(III)$_{(solid)}$ and Fe(II)$_{(aq)}$ with variably depleted $\delta^{56}Fe$ values in the generated dissolved phase (Beard et al., 1999; Crosby et al., 2007). Laboratory experiments of magnetite formation by dissimilatory Fe(III) reduction also demonstrate that isotopic exchange between magnetite and Fe(II)$_{(aq)}$ may be rapid, and that on a mass-balance basis, the bulk $\delta^{56}Fe$ value of magnetite is largely inherited from the precursor ferric oxyhydroxide minerals (Johnson et al., 2005). In general, partial Fe(III) reduction by dissimilatory Fe(III) reduction would likely produce low $\delta^{56}Fe$ values, typically −0.5 and −2.5‰ lower than those of the initial ferric oxyhydroxides (Johnson et al., 2008). However, if complete conversion occurs, the $\delta^{56}Fe$ values of magnetite produced by dissimilatory Fe(III) reduction will be identical to those of the ferric oxyhydroxide precursors. Interestingly, magnetite in the Yuanjiacun oxide-facies BIF has consistently positive $\delta^{56}Fe$ values, similar to those of hematite. This pattern suggests that the magnetite may have inherited the isotopic composition of the ferric oxyhydroxide precursors, followed by complete conversion to magnetite through dissimilatory Fe(III) reduction. The low organic carbon content in the oxide-rich BIF samples further supports the premise that any oxidizable organic carbon deposited with the ferric oxyhydroxide precipitates was consumed during dissimilatory Fe(III) reduction.

2. Magnetite can be the metamorphic by-product of a reaction between hematite and siderite, at temperatures of 480° to 650°C and pressures of 4 and 15 kbars (Koziol, 2004):

$$FeCO_{3(siderite)} + Fe_2O_{3(hematite)}$$
$$= Fe_3O_{4(magnetite)} + CO_2. \qquad (2)$$
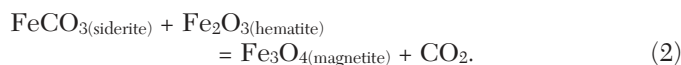
Tian et al. (1986) suggested that the peak P-T conditions for the formation of the chlorite schist associated with the BIF are 2 to 3 kbars and 400° to 450°C, which would have been insufficient for the above reaction to take place. However, the oxidation of dissolved Fe(II), or of Fe(II) minerals such as

siderite, could also drive magnetite production and possibly produce methane in the process (French, 1971) under burial conditions of 450°C and 2 kbars (McCollom, 2003):

$$12FeCO_3 + 2H_2O \rightarrow 4Fe_3O_4 + 11CO_2 + CH_4. \qquad (3)$$

Accordingly, this process could be responsible for formation of the magnetite overgrowths on ankerite (Fig. 7F).

3. The reactions between Fe(II)-rich hydrothermal fluids (<200°C and H_2S poor) and preexisting hematite could form magnetite (Ohmoto, 2003) in environments of limited organic carbon supply. Reaction of dissolved Fe(II) with ferric oxyhydroxide has been shown to yield isotopically heavy oxide phases through the preferential sorption of ^{56}Fe onto Fe oxide surfaces (Icopini et al., 2004). In a similar manner, low $\delta^{56}Fe$ values predicted for Archean seawater may reflect preferential sequestration of ^{56}Fe on ferric oxyhydroxides (e.g., Rouxel et al., 2005). Therefore, it is also possible that the positive $\delta^{56}Fe$ values observed in magnetite from the Yuanjiacun BIF were generated via a hydrothermal Fe^{2+} component ($\delta^{56}Fe \approx 0‰$) reacting with precursor ferric oxyhydroxide precipitates ($\delta^{56}Fe > 0‰$).

Ankerite is commonly associated with the silica-rich microbands. Although some ankerite may have formed penecontemporaneously with early ferric oxyhydroxide precipitates, petrographic evidence suggests that ankerite growth occurred during diagenesis. For example, ankerite is not found within hematite and magnetite grains, whereas small magnetite grains occur as inclusions within the ankerite (Fig. 7H). Ankerite is also preferentially concentrated where several Fe oxide layers coalesce due to burial compaction, forming irregular aggregates that distort the primary microlamination (Fig. 7G). Furthermore, the edges of ankerite commonly display corrosion gulfs resulting in xenomorphic morphology (Fig. 7H). These features imply a late-stage growth of the mineral. One possible reaction is via siderite dissolution and ankerite precipitation (Pecoits et al., 2009; Li, 2014):

$$2FeCO_3 + Ca^{2+} \rightarrow CaFe(CO_3)_2 + Fe^{2+}. \qquad (4)$$

The highly negative $\delta^{13}C$ values of ankerite (average –6.91‰) in the Yuanjiacun BIF, which are consistent with previously determined $\delta^{13}C$ values of siderite in the Yuanjiacun carbonate-facies BIF (average –7.1‰; Tian et al., 1986), strongly suggest that precursor siderite formed by dissimilatory Fe(III) reduction (e.g., Kaufman, 1996; Beukes and Gutzmer, 2008). Moreover, the Fe oxide-facies BIF in the Yuanjiacun sequence contains similar Al_2O_3 concentrations but less organic carbon than the carbonate-rich BIF (Table 2), which is attributed to effective degradation of organic matter in an oxygen-bearing water column before it could be incorporated into the sediment. An alternative interpretation is that hematite-rich BIF was only preserved if the organic carbon influx was low relative to ferric oxyhydroxide accumulation. Under conditions of complete ferric oxyhydroxide reduction, two sources of C are required for siderite formation:

$$4Fe(OH)_3 + CH_2O + 3HCO_3^-$$
$$\rightarrow 4FeCO_3 + 3OH^- + 7H_2O. \qquad (5)$$
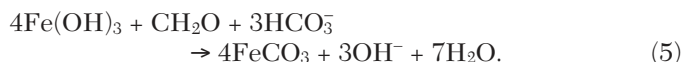
The excess HCO_3^- required in this reaction likely came from seawater infiltration into soft sediment, below the seawater/sediment interface (Heimann et al., 2010). The isotopic composition of HCO_3^- in seawater is assumed to have a $\delta^{13}C$ value of 0‰ (Faure, 1986; Fischer et al., 2009; Bekker et al., 2013; Smith et al., 2013), and we assume that organic carbon (CH_2O) input to the seafloor had a $\delta^{13}C$ value of –24‰, based on the average $\delta^{13}C$ value for organic carbon in the Yuanjiacun BIF. For the above reaction (5), the lowest possible $\delta^{13}C$ value is ca. –6‰ for siderite whose Fe was entirely sourced by dissimilatory Fe(III) reduction. The majority of $\delta^{13}C$ values for ankerite in transition-facies BIF scatter about the $\delta^{13}C$ value predicted by this reaction, suggesting near-complete reduction of $Fe(OH)_3$ by abundant $3HCO_3^-$. Formation of siderite (now ankerite), relative to magnetite, is favored at high P_{CO_2} (Beukes and Gutzmer, 2008). The close spatial relationship between these two minerals in the carbonate-rich BIF (Fig. 7H) suggests that pore water P_{CO_2} may have fluctuated locally between the stability fields of magnetite and siderite. In addition, it is also in open diagenetic environments of the compacted mesobands that the excess organic carbon may be available, such that dissimilatory Fe(III) reduction could easily take place, thus explaining the presence of considerable amounts of ankerite on the outside of chert pods (Fig. 6C).

The depletion in $\delta^{18}O$ values of ankerite in the BIF relative to that of other BIFs (Table 4) can be explained through metamorphic reequilibration or interaction with meteoric water, as indicated by independent evidence that metamorphism (Miyano and Beukes, 1984) in the metasedimentary rocks associated with the Yuanjiaucn BIF exceeded 170°C (Yu et al., 1997) and the fact that interbedded quartz has low $\delta^{18}O$ values ranging between 10.4 and 13.2‰ (Hou et al., 2014).

The most common iron silicates in the BIF are stilpnomelane and chlorite. Stilpnomelane is a characteristic mineral of iron formations that have undergone low- to medium-grade metamorphism (Klein, 2005). It is likely that stilpnomelane was derived from an Fe-rich, but Al-poor silicate precursor such as nontronite, which is itself readily synthesized at low temperature from amorphous ferric oxyhydroxides and dissolved silica under anoxic conditions (Dekov et al., 2007; Rasmussen et al., 2013a; Bekker et al., 2013):

$$2Fe(OH)_3 + 4Si(OH)_4$$
$$\rightarrow Fe_2Si_4O_{10}(OH)_2 \cdot 10H_2O. \qquad (6)$$
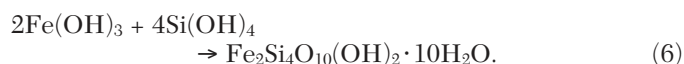
Precursors to chlorite may have been aluminous detrital clay minerals that recrystallized to chlorite during metamorphism. The coexistence of some chlorite and relics of stilpnomelane (Fig. 6G) further suggests that chlorite can be produced by the reaction between stilpnomelane and original Al-rich detritus.

Among the Fe-rich silicates in the Yuanjiacun BIF, minnesotaite and amphibole are generally not as abundant as stilpnomelane. These two minerals typically cut fine-grained sheaves of stilpnomelane (Figs. 6F, 7D-E), suggesting that stilpnomelane became unstable and was then partially transformed into late-stage minnesotaite and amphibole during metamorphism. In addition, calcite is commonly intergrown with amphibole (Fig. 7E). Thus, it is possible that amphibole is also a reaction product of iron-rich carbonates (e.g., ferrodolomite) and quartz, together with calcite (Klein, 2005).

Marine redox structure

The three BIF samples (YJC3-3, YJC4-1, and YJC4-4) contain distinct signatures of terrigenous input, as reflected by

the high modal content of chlorite, and by high but variable concentrations of Al_2O_3, HFSEs (e.g., Zr, Hf), and strong positive correlations between Al_2O_3, TiO_2, and HFSEs. These detrital components within the silicate-facies BIF exclude an abyssal plain fraction because of the low expected influx of allochthonous detritus in such settings (Haugaard et al., 2013). Moreover, the presence of oolitic/granular hematite (Tian et al., 1986) argues for a shallow-water environment. Therefore, a favored depositional site for these samples is more proximal to the paleoshoreline, possible on the shallow shelf.

The REE patterns of relatively siliciclastic-free BIF have frequently been used as a qualitative proxy of paleoseawater redox conditions (Bau, 1999; Slack et al., 2007; Pecoits et al., 2009; Planavsky et al., 2010; Haugaard et al., 2013). Moreover, the REEs + Y in BIF are generally regarded as being immobile during most geologic processes (e.g., Bingen et al., 1996), and effects of metamorphism on the REE distribution in BIF have been found to be only of minor importance in most cases (Bau and Dulski, 1996). Accordingly, the distribution of Y and REEs observed in the detritus-free Yuanjiacun BIF samples reflects those present in the primary marine precipitates. In this context, the BIF samples display consistently positive La and Y anomalies, depletion of LREEs and MREEs relative to HREEs, and superchondritic Y/Ho ratios (>26); these collectively are features typical of modern seawater (Fig. 8). The positive Y anomalies in the BIF are distinct from those of slowly growing, modern marine hydrogenetic ferromanganese deposits that have negative Y anomalies, instead being more similar to rapidly precipitated, modern marine hydrothermal ferromanganese deposits. We thus infer that BIF precipitation occurred very rapidly and that the scavenged REE were not in exchange equilibrium with ambient seawater (see Bau and Dulski, 1996). Rapid precipitation strongly favors a scenario for deposition of the BIF in which precipitation occurred due to upwelling of reduced ferruginous waters into an oxygenated shallow-water setting.

In contrast to modern seawater, the various Yuanjiacun BIF facies display positive Eu anomalies, which were sourced from high-temperature (>350°C) hydrothermal fluids effused after alteration of ocean-floor basalt (Fig. 8; Beukes et al., 1990; Bau, 1993; Bau and Dulski, 1996; Kato et al., 1998). This process suggests one of the following scenarios (1) much of the water column in the basin contained hydrothermally derived REEs; (2) the hydrothermal fluids welled up onto the shelf, perhaps as part of a plume (Isley, 1995), which facilitated BIF precipitation, i.e., the BIF did not precipitate from ambient seawater; or (3) hydrothermal vents were proximal to the site of BIF deposition. In any case, enhanced magmatic activity (e.g., during eruption of large igneous provinces) would have created the ferruginous redox conditions in the oceans that promoted large-scale transport of dissolved iron (Bekker et al., 2010, 2013). In addition, such processes would have caused marked sea-level rise and transgressions, which in turn favored deposition of BIF on drowned, sediment-starved, continental shelves (e.g., Isley and Abbott, 1999).

The redox-sensitive REEs, Eu and Ce, are often used to provide insights into the redox state of ancient seawater, and also the level of atmospheric oxygenation at that time (e.g., Frei et al., 2008). Modern oxygenated seawater shows a strong negative Ce anomaly and LREE depletion relative to HREE,

using REE data that are normalized to the composition of average shale. By contrast, suboxic and anoxic waters lack negative Ce anomalies (German and Elderfield, 1990; Byrne and Sholkovitz, 1996) and display elevated LREE to HREE ratios. The cause of REE patterns in oxygenated seawater is oxidation of trivalent Ce that greatly reduces Ce solubility, resulting in preferential removal onto Mn-Fe oxyhydroxides, organic matter, and clay particles. Additionally, light REEs relative to heavy REEs are preferentially removed onto Mn-Fe oxyhydroxides and other reactive surfaces due to differential REE particle reactivity linked with REE carbonate complexation (Planavsky et al., 2010). In suboxic and anoxic waters, negative Ce anomalies are absent, or are locally positive due to the reductive dissolution of Mn-Fe oxyhydroxides below the redoxcline, resulting in an increased ratio of LREEs to HREEs (German et al., 1991; Sholkovitz et al., 1992). Moreover, based on experimental results, there is negligible oxidative scavenging of Ce onto ferric oxyhydroxide surfaces, unlike Mn(III/IV) oxides at pH conditions >5 (Bau, 1999; Ohta and Kawabe, 2001). Therefore, ferric oxyhydroxides qualitatively record Ce anomalies from the water column from which they precipitated, whereas Mn(III/IV) oxides are influenced by preferential Ce scavenging (Planavsky et al., 2009).

In combination with previous REE data for the Yuanjiacun magnetite-rich units (Wang et al., 2014), the Yuanjiacun BIF samples display a shift from positive or nonexistent to slightly negative Ce anomalies (Fig. 9), indicating the presence of a strong redoxcline (Planavsky et al., 2010). Specifically, the presence of small negative Ce anomalies in the hematite-rich units may imply mildly oxidizing conditions in shallow waters, due to limited Ce oxidation and sorption onto Mn oxyhydroxides. However, the remaining BIF samples lack significant Ce anomalies, suggesting that the BIF formed mainly in low oxygen environments, below, or at, the redoxcline. The positive Eu anomalies in the BIF are consistent with widespread anoxia (Kamber and Webb, 2001).

Variability in ratios of light to heavy REE $((La/Yb)_{SN})$ in samples of the Yuanjiacun BIF might also reflect formation below, or at, a redoxcline (Wang et al., 2014). Redox-dependent Mn cycling in the suboxic zone can dramatically alter REE patterns by decreasing the level of light REE depletion (German and Elderfied, 1990). This interpretation implies that precipitation of iron occurred in water masses having a varying contribution of REEs from the dissolution of Mn oxyhydroxides. The lower detrital element concentrations (e.g., Al_2O_3) and lack of correlation between ratios of LREEs to HREEs and Al_2O_3 rule out the possibility that the siliciclastic input is the predominant control over the trivalent REE patterns (Planavsky et al., 2009).

It is worth noting that except for the slightly negative Ce anomalies (Fig. 9), the REE patterns of the Yuanjiacun BIF are similar to those of late Paleoproterozoic (<2.0 Ga) iron formations, but differ from those in iron formations prior to the GOE (Planavsky et al., 2010). The large range of Ce anomalies and ratios of LREEs to HREEs in the BIF might reflect varying effects of the precipitation/dissolution of a Mn oxyhydroxide shuttle, from shallow-water oxidized settings to deeper water-reducing environments (Wang et al., 2014).

Iron isotopes in BIF have been used to trace Fe cycling and fingerprint redox processes that led to deposition of BIF

(Johnson et al., 2003, 2008; Rouxel et al., 2005; Anbar and Rouxel, 2007). The most common mechanism proposed for accumulation of iron-rich components in BIF is the oxidation of hydrothermally sourced $Fe(II)_{(aq)}$ (Klein, 2005), which should produce a $\delta^{56}Fe$ value of ca. 0‰, or slightly negative (−0.5‰; Johnson et al., 2008; Planavsky et al., 2012a). Iron oxyhydroxides that precipitated under fully oxygenated conditions are expected to have the same $\delta^{56}Fe$ value as the dissolved iron sources, because of nearly complete Fe(II) oxidation and Fe(III) mineral precipitation. In contrast, partial Fe(II) oxidation produces iron oxyhydroxides with positive $\delta^{56}Fe$ values relative to the Fe(II) source. The presence of positive $\delta^{56}Fe$ values for hematite and magnetite in the Yuanjiacun oxide-facies BIF (Table 5) thus points to incomplete Fe(II) oxidation, which by extension, suggests deposition under conditions of low oxygenation.

BIF depositional model

Detailed lithostratigraphic information (Shen et al., 1982; Tian et al., 1986; Zhu et al., 1988) in combination with geochemical data permit us to reconstruct a potential depositional model for the Yuanjiacun BIF (Fig. 10). The system tract for this BIF begins near shore with thickly bedded, wave-rippled, and cross-stratified quartz sandstone that was deposited above normal wave base (Fig. 4). The distribution of lithologic units in upward-fining increments indicates that hematite-magnetite (oxide facies) BIF and associated meta-arenites and shales mark the beginning of transgression, whereas the oolitic/granular hematite (Zhu et al., 1988) is indicative of deposition in near-shore, shallow waters. The fact that the iron formations form the base of coarsening-upward progradational increments of sedimentation also implies that they were likely deposited most distal from siliciclastic input during transgression. Close examination of the vertical facies of

the Yuanjiacun BIF reveals that the hematite-magnetite facies typically grades upward into magnetite-silicate and silicate-siderite facies, indicating that carbonate-rich iron formation was likely deposited in the most distal part of the depositional basin, during peaks of transgression, followed shoreward by hematite-magnetite facies iron formation. This distinct vertical facies change is also observed laterally, from west to east, i.e., the iron mineral assemblage changes from siderite through silicate into magnetite and hematite iron formations (Fig. 2C).

The alternating iron- and silica-rich microbands in the BIF, without indication of current activity, could reflect stable basinal conditions with precipitation occurring below storm-wave base (ca. 200 m), which is the average depth of the modern storm-wave base (Boggs, 1995). However, the local presence in the Yuanjiacun oxide-facies BIF of current-generated structures, such as crossbedding and granular textures (Tian et al., 1986), indicates that this facies formed in somewhat shallower environments at depths where storm-wave currents could occasionally rework bottom sediments. It should be noted that the carbonate-facies BIF is closely associated with the beds of stilpnomelane lutite (Fig. 4), which may represent ferruginized felsic pyroclastic material (Zhu et al., 1988). Additionally, positive Eu anomalies in the carbonate-rich iron formation are more pronounced than those in the oxide- and silicate-facies BIFs (Table 1). This pattern suggests that hydrothermal fluids related to volcanic events influenced the entire depositional environment for iron, and that the carbonate-facies BIF was more likely to have been deposited closer to submarine hydrothermal vents.

The Yuanjiacun BIF displays a clear REE signature indicative of basin-scale redox stratification and Fe(III) formation under varying redox conditions (Fig. 10). Specifically, a wide range of true Ce anomalies, varying from slightly negative to
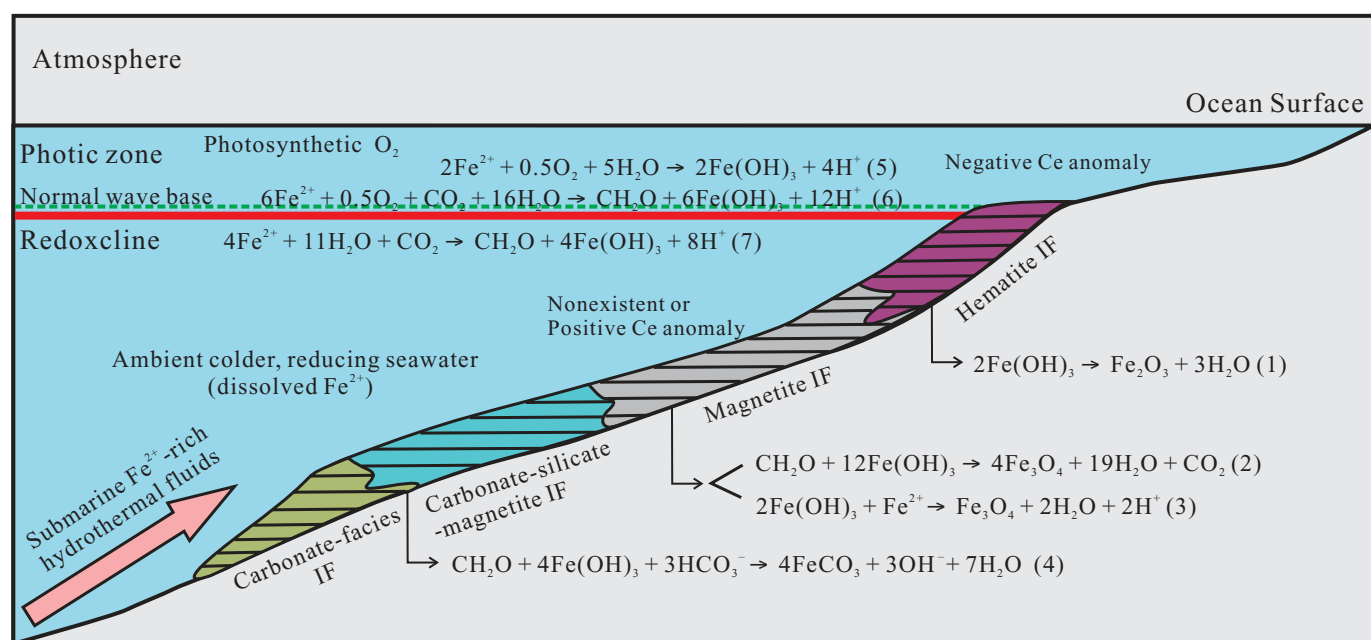

FIG. 10. Conceptual depositional model for the Paleoproterozoic Yuanjiacun BIF. Reactions (2) and (3) are adapted from Beukes and Gutzmer (2008) and Ohmoto (2003), respectively; reaction (4) is modified from Heimann et al. (2010). Reaction (6) is from Konhauser et al. (2002), and reaction (7) is adapted from Kappler et al. (2005). IF = iron formation.

positive, or nonexistent, and range of LREE to HREE ratios present in the oxide-facies BIF, indicate that this facies formed in both mildly oxic shallow seawater and deeper anoxic waters, in contrast to the silicate- and carbonate-facies BIFs that lack Ce anomalies and thus likely formed in relatively deep, reducing waters. A dynamic redoxcline must have separated the oxic upper part of the water column from suboxic to anoxic deeper parts. This redox stratification, in combination with the formational age of the Yuanjiacun BIF (~2.38–2.21 Ga; Liu et al., 2012; Liu et al., 2014; Wang et al., 2015), is consistent with global atmospheric oxygenation that occurred between 2.4 and 2.2 Ga (Bekker et al., 2004; Konhauser et al., 2011a).

The actual mechanism of Fe(II) precipitation to form the ferric oxyhydroxide precursors to BIF remains a subject of debate. One possibility is the abiotic oxidation of Fe(II) by the O_2 produced by cyanobacteria (Cloud, 1968; Klein and Beukes, 1993), which may have played a role in depositing ferric oxyhydroxides in parts of the Yuanjiacun oxide-facies BIF in shallow oxic environments. Alternatively, the direct oxidation of Fe(II) by ancient microorganisms could have taken place by microaerophilic Fe(II) oxidizers, using cyanobacterially-produced O_2 as an electron acceptor (Emerson and Revsbech, 1994; Konhauser et al., 2002), or anoxygenic phototrophic Fe(II) oxidizers that use light to oxidize Fe(II) in the absence of O_2 (Kappler et al., 2005; Posth et al., 2008). The stratigraphy and lateral facies reconstruction of the Yuanjiacun BIF suggest that most of this iron-rich sequence was deposited below storm-wave base, but this model does not constrain where the initial Fe(II) oxidation took place. In other words, Fe(II) would have been oxidized in the photic zone, and the resultant ferric oxyhydroxide particles would then have fallen through the water column to the seafloor, irrespective of whether that setting represented very shallow or deep waters. However, what is telling is that a biologically mediated Fe(II) oxidation process must have required sufficient nutrients to support the microbial biomass.

Within iron formation beds, the lateral facies changes are well represented by the presence of ferric oxyhydroxides with minor silica occurring most distal from volcanic centers or hydrothermal vents, versus the carbonate (siderite)- and silicate-rich assemblages that formed more proximal to the inferred vent sites (Fig. 10). The decrease in carbonates and increase in magnetite and hematite toward the former shoreline (i.e. more distal from hydrothermal vents) suggests that the supply of organic carbon to the sediment decreased in this direction (Beukes and Gutzmer, 2008; Köhler et al., 2013). This interpretation is in contrast to previous models of BIF deposition, such as for the 2.46 Ga Kuruman Iron Formation in South Africa, in which hematite represents the most deep water facies where organic carbon supply was so low that dissimilatory Fe(III) reduction did not occur, while siderite precipitated in a near-shore setting where organic carbon supply was abundant (Beukes et al., 1990). These different models can be explained by the location of primary productivity. In the Kuruman Iron Formation, the BIF conformably underlies shallow-water, organic-rich carbonates and shales, suggesting that the carbon source came from areas of high photosynthetic primary productivity and abundant nutrients on the shallow carbonate shelf, and by extension, that the nutrients

for the microbial mats (e.g., chemolithoautotrophic iron-oxidizing bacteria) had a terrestrial source. By contrast, primary productivity in the Yuanjiacun basin seems to have been more prevalent in deeper water settings, implying that nutrients (e.g., V, Fe, Co, and Zn) were most likely sourced from marine hydrothermal vents. Therefore, in settings proximal to vent sites, organic matter supply outpaced degradation, and more organic matter thus reached the sediment surface, resulting in effective dissimilatory Fe(III) reduction and the formation of early diagenetic siderite and magnetite. By contrast, depositional areas more distal from vent sites had very low primary organic productivity, allowing ferric oxyhydroxides to accumulate on the seafloor of the depository, to be later transformed into hematite and/or magnetite (Fig. 10). Perhaps the most intriguing aspect of this model is that the shallow waters did not contain an abundant plankton biomass, and if this was the case, then the most likely oxidant for the oolitic/granular hematite (Tian et al., 1986), and parts of hematite-rich BIF, was O_2. This interpretation suggests that oxidation of Fe(II) was indirectly linked to cyanobacteria, and that the cyanobacteria were not necessarily abundant at the site of Fe(II) oxidation. In other words, the shallow waters were sufficiently oxygenated at this time such that any shallow-water Fe(II) was rapidly oxidized.

Silica would have been introduced together with ferrous iron from hydrothermal deep water (Bekker et al., 2013; Hou et al., 2014), and its precipitation is brought about by a decrease in temperature in the zone where the slightly warmer water mixes with cold ambient seawater (Beukes and Gutzmer, 2008). But given that ambient seawater in the Precambrian had a high silica content (e.g., Siever, 1992), hence in settings distal from hydrothermal vents—like that for the Yuanjiacun BIF—a local seawater source for the silica is also possible. In addition, we propose that in environments of low organic carbon burial, in the presence of dissolved Fe(II) (Harder, 1976, 1978), nontronite (precursor to stilpnomelane) is readily precipitated from mixtures of amorphous iron oxyhydroxides and silica under low-temperature anoxic conditions, resulting in a scattered distribution of the silicate-facies BIF between the oxide- and carbonate-facies BIFs.

The Yuanjiacun BIF and global environmental conditions

Previous studies have concluded that giant iron formations (≥10,000 Gt) were not deposited between ca. 2.4 and 2.0 Ga (e.g., Bekker et al., 2010). Iron formations of this time period are distinctly different in scale (i.e., smaller), and in most cases their depositional settings are similar to those of Archean BIF. It seems that from ca. 2.4 to 2.0 Ga, either the deep-ocean redox state was too oxidized, relative to the magnitude of hydrothermal input, to have the ferruginous deep waters needed to promote the formation of giant BIFs, or that marine sulfate levels were high enough so that the sulfide produced during bacterial sulfate reduction exceeded the hydrothermal Fe(II) supply, with the result that iron sulfides precipitated instead of iron oxides (see Kump and Seyfried, 2005). Several independent lines of evidence point toward high sulfate levels (>2.5 mM) during the Lomagundi Event at 2.22 to 2.11 Ga (Bekker et al., 2006; Schröder et al., 2008; Planavsky et al., 2012b; Scott et al., 2014), consistent with the idea that growth of the marine sulfate reservoir challenged the hydrothermal

iron flux, and ultimately exerted a first-order control on the distribution and abundance of iron formations.

Oolitic hematitic ironstones of the Paleoproterozoic Timeball Hill Formation in South Africa were deposited in shallow-water, above fair-weather wave base (Schweigart, 1965; Dorland, 1999). Few geochemical data are available for this unit, partly because it contains significant amounts of siliciclastic material. Its deposition at ca. 2.32 Ga (Hannah et al., 2004; Rasmussen et al., 2013b) may coincide with a magmatic event at that time (e.g., Berman et al., 2005; Hartlaub et al., 2007). However, the significance of this magmatic event is poorly known. Another possible BIF that was deposited in this time interval is the 2.3 Ga Hotazel Formation in South Africa, although its depositional age remains controversial (Gutzmer and Beukes, 1997). Tsikos and Moore (1997) conducted geochemical studies on 12 samples of iron formation from this BIF and found an absence of positive Eu anomalies and negative Ce anomalies. However, by using the approach of Bau and Dulski (1996) to discriminate true Ce anomalies, we find that only two of the 12 Hotazel BIF samples have Ce anomalies, both of which are slightly negative. Because most of the data for these samples lack Tb values, we cannot calculate Eu anomalies. Nonetheless, the original calculation method indicates that some samples have slightly positive Eu anomalies (shale-normalized basis). Hence, we suggest that the REE patterns of the Hotazel BIF are similar to those of the Kuruman BIF, except for lower Eu anomalies in the former (Bau and Dulski, 1996). The presence of these Eu anomalies implies a dilute hydrothermal signature rather than an oxygenated state for the coeval deep ocean at ca. 2.3 Ga.

The ~2.38 to 2.21 Ga Yuanjiacun BIF is likely to be the largest (>1,000 Gt) and most extensive BIF known during this globally, BIF-poor time interval. This BIF is likewise associated with transgression and consists of three upward-deepening to upward-shallowing sequences that were deposited in a continental shelf environment. Significantly, the Yuanjiacun BIF displays prominent positive and negative Ce anomalies and large shale-normalized ratios of LREEs to HREEs, which are essentially absent in pre-GOE iron formations (Planavsky et al., 2010). These features suggest that the ancient ocean at that time was redox-stratified, from oxic shallow waters to deeper anoxic waters. This marked redox stratification contrasts with the widespread, low-oxidizing potential that existed in the pre-GOE ocean. The presence of consistently positive Eu anomalies is also important, indicating that the global ocean was dominated by a high-temperature hydrothermal flux at that time. Episodic delivery of Fe from hydrothermal fluids into the oceans could have had dramatic impacts on ocean productivity and ecosystem structure.

Deposition of the Yuanjiacun BIF occurred sometime during the GOE, but predates the largest positive carbon isotope excursion in Earth's history, the 2.22 to 2.11 Ga Lomagundi Event, which appears to be related to high burial rates of organic carbon and associated oxygen release to the atmosphere (e.g., Schidlowski et al., 1976; Karhu and Holland, 1996; Bekker et al., 2001; Bekker and Holland, 2012). The gaps in the record of major Superior-type iron formations deposition at 2.3 to 2.2 Ga closely coincide with inferred pauses in global plate tectonic activity (Silver and Benn, 2008; Condie et al., 2009). The diagnostic REE pattern and geologic features observed in the Yuanjiacun BIF may, therefore, indicate that significant parts of the shallow oceans were already oxygenated by ~2.3 Ga and that Fe(II) was soluble only in lower reduced waters of local basins overwhelmed by a relatively intense hydrothermal flux of reduced components such as Fe, Mn, and H_2S.

During the Lomagundi carbon isotope excursion, sedimentrary sequences such as those containing hematitic oolites and hematite-rich sandstones in South Africa (e.g., Silverton Formation; Schweigart, 1965) and on the Kola Peninsula in Russia (Kuetsjärvi Sedimentary Formation; Akhmedov, 1972a) were attributed to be deposited in shallow-marine environments. The BIFs deposited during the 2.22 to 2.11 Ga Lomagundi excursion include those within the Ijil Group, Mauritania (Bronner and Chauvel, 1979), and the Lomagundi Group, Zimbabwe (Master, 1991). The former belongs to the 2.20 to 2.10 Ga Birimian basin in West Africa, which also contains iron and manganese formations in the Francevillian basin, Gabon, and in the Nigerian schist belts. The latter developed within the ca. 2.2 to 2.1 Ga Magondi belt. During the same time period, several volcanic-hosted iron formations were deposited in Brazil (e.g., Aimbé Formation, Guarinos Group; Resende and Jost, 1995; and Itapicuru Complex of the Rio Itapicuru greenstone belt; Dalton de Souza et al., 2003) and Norway (Iddjajav'ri Group, Karasjok greenstone belt; Often, 1985).

Immediately after the Lomagundi carbon isotope excursion, small, volcanic-hosted iron formations in North America (e.g., Homestake Iron Formation, Black Hills, South Dakota; Frei et al., 2008) and Finland (Paakola, 1971; Laajoki and Saikkonen, 1977) were deposited in several basins. Oolitic hematitic ironstone also formed within the Kolasjoki Formation, Kola Peninsula, Russia (Akhmedov, 1972b). Taken together, these data are tentatively interpreted as recording dynamic ocean redox conditions that were constructed in the aftermath of the GOE, with periodic upwelling of iron into shallow-water settings above storm and fair-weather wave base. Interestingly, the 2.1 to 2.0 Ga BIF in the Black Hills displays REE patterns similar to those of the Yuanjiacun BIF, in which both positive and negative Ce anomalies are present (Frei et al., 2008). These features in the Black Hills BIF have been attributed to supergene oxidative processes and the oxygenation of bottom seawaters (Frei et al., 2008). This explanation has not been tested so far and requires further consideration.

An exciting, and perhaps unexpected, finding to come out of recent studies on secular trends in trace metal contents of BIF (and black shale) is that Earth's redox fabric may have been more complicated than previously thought. For example, Partin et al. (2013a, b) have shown that directly following a dramatic increase in the oceanic U reservoir during the GOE, this reservoir decreased significantly after 2.10 Ga, resulting in U contents in BIF and shales that are only marginally higher than those of pre-GOE levels. Given that the oxygen content of the atmosphere directly controls U supply via oxidative weathering, this decrease in U contents could be due to a subsequent drop in the level of atmospheric oxygenation following the Lomagundi Event. It certainly seems plausible that the burial of organic carbon associated with oxygen production during the Lomagundi Event later became an oxygen sink as the organic matter became oxidized, driving oxygen

to low levels that may have persisted for hundreds of million years (Bekker and Holland, 2012; Canfield et al., 2013).

In summary, our observations are consistent with a model wherein the presence of BIF between 2.3 and 2.0 Ga suggests a redox-stratified ocean during and immediately after the GOE, and that the presence of hematite granules (Tian et al., 1986; Zhu et al., 1988) implies a high oxidizing potential of shallow-water environments. The bottom waters were reduced and sulphur poor, and Fe(II) that was introduced via hydrothermal emanations also would have maintained high iron levels in the waters of local basins.

Conclusions

Integration of sedimentologic, petrographic, geochemical, and isotopic data indicates that the ~2.38 to 2.21 Ga Yuanjiacun BIF formed in the upper oxygenated photic zone of a predominantly ferruginous deep ocean. Iron could have been precipitated inorganically through reaction with photosynthetically derived free oxygen in shallow waters, while in deeper water environments, under microaerobic conditions, chemolithoautotrophic Fe(II)-oxidizing or photoferrotrophic bacteria facilitated the deposition of ferric oxyhydroxides. The lateral and vertical facies changes in the Yuanjiacun BIF are represented by oxide-facies BIF near shore, and carbonate (siderite)- and silicate-facies assemblages in deeper waters. The fact that the more ferrous BIF facies formed in deeper waters (which implies dissimilatory iron reduction via organic carbon oxidation) suggests that primary productivity was likely higher offshore than near the continents. Given the low clastic contribution to the BIF, the source of nutrients for the plankton might have come from submarine hydrothermal fluids. If these assumptions are correct, then this model further suggests that the shallow waters were already sufficiently oxygenated such that Fe(II) oxidation near shore was not directly tied to the presence of local cyanobacteria. Results of this study of the Yuanjiacun BIF therefore might represent direct proof for the expansion, at ~2.38 to 2.21 Ga, of oxygen oases into more oxygenated surface oceans.

Acknowledgments

REFERENCES

Akhmedov, A.M., 1972a, Iron-rich metasedimentary rock of Pechenga Complex and their genesis: Materials on geology and metallogeny of Kola Peninsula: Apatity, v. 4, p. 125–131 (in Russian).
——1972b, Hematite oolites in sedimentary rocks of the Pechenga Complex: Materials on mineralogy of the Kola Peninsula: Nauka, v. 9, p. 135–137 (in Russian).

Anbar, A.D., and Rouxel, O., 2007, Metal stable isotopes in paleoceanography: Annual Review of Earth and Planetary Sciences, v. 35, p. 717–746.
Bau, M., 1993, Effects of syn- and post-depositional processes on the rare-earth element distribution in Precambrian iron-formations: European Journal of Mineralogy, v. 5, p. 257–267.
——1999, Scavenging of dissolved yttrium and rare earths by precipitating Fe oxyhydroxide: Experimental evidence for Ce oxidation, Y-Ho fractionation, and lanthanide tetrad effect: Geochimica et Cosmochimica Acta, v. 63, p. 67–77.
Bau, M., and Dulski, P., 1996, Distribution of yttrium and rare-earth elements in the Penge and Kuruman iron-formations, Transvaal Supergroup, South Africa: Precambrian Research, v. 79, p. 37–55.
——1999, Comparing yttrium and rare-earth in hydrothermal fluids from the Mid-Atlantic Ridge: Implications for Y and REE behaviour during near vent mixing and for the Y/Ho ratio of Proterozoic seawater: Chemical Geology, v. 155, p. 77–90.
Beard, B.L., Johnson, C.M., Cox, L., Sun, H., Nealson, K.H., and Aguilar, C., 1999, Iron isotope biosignatures: Science, v. 285, p. 1889–1892.
Bekker, A., and Holland, H.D., 2012, Oxygen overshoot and recovery during the early Paleoproterozoic: Earth and Planetary Science Letters, v. 317–318, p. 295–304.
Bekker, A., Kaufman, A.J., Karhu, J.A., Beukes, N.J., Swart, Q.D., Coetzee, L.L., and Eriksson, K.A., 2001, Chemostratigraphy of the Paleoproterozoic Duitschland Formation, South Africa: Implications for coupled climate change and carbon cycling: American Journal of Science, v. 301, p. 261–285.
Bekker, A., Holland, H.D., Wang, P.L., Rumble, III, D., Stein, H.J., Hannah, J.L., Coetzee, L.L., and Beukes, N.J., 2004, Dating the rise of atmospheric oxygen: Nature, v. 427, p. 117–120.
Bekker, A., Karhu, J.A., and Kaufman, A.J., 2006, Carbon isotope record for the onset of the Lomagundi carbon isotope excursion in the Great Lakes area: Precambrian Research, v. 148, p. 145–180.
Bekker, A., Slack, J.F., Planavsky, N., Krapež, B., Hofmann, A., Konhauser, K.O., and Rouxel, O.J., 2010, Iron formation: The sedimentary product of a complex interplay among mantle, tectonic, oceanic, and biospheric processes: Economic Geology, v. 105, p. 467–508.
Bekker, A., Krapež, B., Slack, J.F., Planavsky, N., Hofmann, A., Konhauser, K.O., and Rouxel, O.J., 2012, Iron formation: The sedimentary product of a complex interplay among mantle, tectonic, oceanic, and biospheric processes—a reply: Economic Geology, v. 107, p. 379–380.
Bekker, A., Planavsky, N.J., Krapež, B., Rasmussen, B., Hofmann, A., Slack, J.F., Rouxel, O.J., and Konhauser, K.O., 2013, Iron formation: Their origins and implications for ancient seawater chemistry, in Mackenzie, F.T., eds.,, Sediments, diagenesis, and sedimentary rocks: Amsterdam, Elsevier, Treatise on Geochemistry, 2nd ed. v. 7, p. 561–628. http://faculty.eas.ualberta.ca/konhauser/Reprints/Bekker%20chapter%282014%29.pdf
Berman, R.G., Sanborn-Barrie, M., Stern, R.A., and Carson, C.J., 2005, Tectonometamorphism at ca. 2.35 and 1.85 Ga in the Rae domain, western Churchill Province, Nunavut, Canada: Insights from structural, metamorphic and in situ geochronological analysis of the southwestern Committee Bay belt: Canadian Mineralogist, v. 43, p. 409–442.
Beukes, N.J., and Gutzmer, J., 2008, Origin and paleoenvironmental significance of major iron formations at the Archean-Paleoproterozoic boundary: Reviews in Economic Geology, v. 15, p. 5–47.
Beukes, N.J., Klein, C., Kaufman, A.J., and Hayes, J.M., 1990, Carbonate petrography, kerogen distribution, and carbon and oxygen isotope variations in an Early Proterozoic transition from limestone to iron-formation deposition: Transvaal Supergroup, South Africa: Economic Geology, v. 85, p. 663–690.
Bingen, B., Demaiffe, D., and Hergoten, J., 1996, Redistribution of REE, thorium and uranium over accessory minerals in the course of amphibolite to granulite facies metamorphism: The role of apatite and monazite in orthogneisses from south-eastern Norway: Geochimica et Cosmochimica Acta, v. 60, p. 1341–1354.
Boggs, S., 1995, Principles of sedimentology and stratigraphy: New Jersey, Prentice-Hall, 784 p.
Bolhar, R., Kamber, B.S., Moorbath, S., Fedo, C.M., and Whitehouse, M.J., 2004, Characterisation of Early Archaean chemical sediments by trace element signatures: Earth and Planetary Science Letters, v. 222, p. 43–60.
Bronner, G., and Chauvel, J.J., 1979, Precambrian banded iron-formations of the Ijil Group (Kediat Ijil, Reguibat Shield, Mauritania): Economic Geology, v. 74, p. 77–94.
Byrne, R., and Sholkovitz, E., 1996, Marine chemistry and geochemistry of the lanthanides, in Gschneider, K.A., Jr., and Eyring, L., eds., Handbook

on the physics and chemistry of the rare earths: Amsterdam, Elsevier, v. 23, p. 497–593.

Canfield, D.E., Ngombi-Pemba, L., Hammarlund, E.U., Bengtson, S., Chaussidon, M., Gauthier-Lafaye, F., Meunier, A., Riboulleau, A., Rollion-Bard, C., Rouxel, O., Asael, D., Pierson-Wickmann, A.-C., and El Albani, A., 2013, Oxygen dynamics in the aftermath of the Great Oxidation of Earth's atmosphere: Proceedings of the National Academy of Sciences, v. 110, p. 16,736–16,741.

Chen, D., Qing, H., and Li, R., 2005, The Late Devonian Frasnian-Famennian (F/F) biotic crisis: Insights from $\delta^{13}C_{carb}$, $\delta^{13}C_{org}$, and $^{87}Sr/^{86}Sr$ isotopic systematics: Earth and Planetary Science Letters, v. 235, p. 151–166.

Cloud, P., 1968, Atmospheric and hydrospheric evolution on the primitive Earth: Science, v. 160, p. 729–736.

Condie, K.C., O'Neill, C., and Aster, R., 2009, Evidence and implications for a widespread magmatic shutdown for 250 My on Earth: Earth and Planetary Science Letters, v. 282, p. 294–298.

Craddock, P.R., and Dauphas, N., 2011, Iron and carbon isotope evidence for microbial iron respiration throughout the Archean: Earth and Planetary Science Letters, v. 303, p. 121–132.

Crosby, H.A., Roden, E.E., Johnson, C.M., and Beard, B.L., 2007, The mechanisms of iron isotope fractionation produced during dissimilatory Fe(III) reduction by Shewanella putrefaciens and Geobacter sulfurreducens: Geobiology, v. 5, p. 169–189.

Dai, Y.P., Zhang, L.C., Wang, C.L., Liu, L., Cui, M.L., Zhu, M.T., and Xiang, P., 2012, Genetic type, formation age and tectonic setting of the Waitoushan banded iron formation, Benxi, Liaoning Province: Acta Petrologica Sinica, v. 28, p. 3574–3594 (in Chinese).

Dalton de Souza, J., Kosin, M., Melo, R.C., Oliveira, E.P., Carvalho, M.J., and Leite, C.M., 2003, Guia de excursão—Geologia do segmento norte do orógeno itabuna-salvador-curaçá: Revista Brasileira de Geociências, v. 33 (supplement), p. 27–32.

Dekov, V.M., Kamenov, G.D., Stummeyer, J., Thiry, M., Savelli, C., Shanks, W.C., Fortin, D., Kuzmann, E., and Vertes, A., 2007, Hydrothermal nontronite formation at Eolo Seamount (Aeolian volcanic arc, Tyrrhenian Sea): Chemical Geology, v. 245, p. 103–119.

Dorland, H.C., 1999, Paleoproterozoic laterites, red beds and ironstones of the Pretoria Group with reference to the history of atmospheric oxygen: M.Sc. thesis, Johannesburg, Rand Afrikaans University, 147 p.

Emerson, D., and Revsbech, N.P., 1994, Investigation of an iron-oxidizing microbial mat community located near Aarhus, Denmark: Laboratory studies: Applied and Environmental Microbiology, v. 60, p. 4032–4038.

Ewers, W.E., 1983, Chemical factors in the deposition and diagenesis of banded iron-formation, in Trendall, A.F., and Morris, R.C., eds., Banded iron-formation: Facts and problems: Amsterdam, Elsevier, p. 491–512.

Faure, G., 1986, Principles of isotope geology: New York, Wiley, 589 p.

Fischer, W.W., and Knoll, A.H., 2009, An iron shuttle for deep-water silica in Late Archean and early Paleoproterozoic iron formation: Geological Society of America Bulletin, v. 121, p. 222–235.

Fischer, W.W., Schroeder, S., Lacassie J.P., Beukes, N.J., Goldberg, T., Strauss, H., Horstmann, U.E., Schrag, D.P., and Knoll, A.H., 2009, Isotopic constraints on the Late Archean carbon cycle from the Transvaal Supergroup along the western margin of the Kaapvaal craton, South Africa: Precambrian Research, v. 169, p. 15–27.

Frei, R., Dahl, P.S., Duke, E.F., Frei, K.M., Hansen, T.R., Frandsson, M.M., and Jensen, L.A., 2008, Trace element and isotopic characterization of Neoarchean and Paleoproterozoic iron formations in the Black Hills (South Dakota, USA): Assessment of chemical change during 2.9–1.9 Ga deposition bracketing the 2.4–2.2 Ga first rise of atmospheric oxygen: Precambrian Research, v. 162, p. 441–474.

French, B.M., 1971, Stability relations of siderite ($FeCO_3$) in the system Fe-C-O: American Journal of Science, v. 271, p. 37–78.

Frost, C.D., von Blankenburg, F., Schoenberg, R., Frost, B.R., and Swapp, S.M., 2007, Preservation of Fe isotope heterogeneities during diagenesis and metamorphism of banded iron formation: Contributions to Mineralogy and Petrology, v. 153, p. 211–235.

Garrels, R.M., 1987, A model for the deposition of the micro-banded Precambrian iron formations: American Journal of Science, v. 287, p. 81–106.

Geng, Y.S., Wan, Y.S., Shen, Q.H., Li, H.M., and Zhang, R.X., 2000, Chronological framework of the Early Precambrian important events in the Lüliang area, Shanxi Province: Acta Petrologica Sinica, v. 74, p. 216–223 (in Chinese).

Geng, Y.S., Wan, Y.S., and Yang, C.H., 2008, Integrated research report on the establishment of Paleoproterozoic system of China: Determination of major Paleoproterozoic geological events and preliminary subdivision of Paleoproterozoic strata in the Lüliang area, in National Stratigraphy Commission, eds., Research Report on the Establishment of Major Stratigraphical Stages in China (2001–2005): Beijing, Geological Publishing House, p. 515–533 (in Chinese).

German, C.R., and Elderfield, H., 1990, Application of the Ce anomaly as a paleoredox indicator: The ground rules: Paleoceanography, v. 5, p. 823–833.

German, C.R., Holliday, B.P., and Elderfield, H., 1991, Redox cycling of rare earth elements in the suboxic zone of the Black Sea: Geochimica et Cosmochimica Acta, v. 55, p. 3553–3558.

Gross, G.A., 1980, A classification of iron formations based on depositional environments: Canadian Mineralogist, v. 18, p. 215–222.

Gutzmer, J., and Beukes, N.J., 1997, Effects of mass transfer, compaction and secondary porosity on hydrothermal upgrading of Paleoproterozoic sedimentary manganese ore in the Kalahari manganese field, South Africa: Mineralium Deposita, v. 32, p. 250–256.

Hannah, J.L., Bekker, A., Stein, H.J., Markey, R.J., and Holland, H.D., 2004, Primitive Os and 2316 Ma age for marine shale: Implications for Paleoproterozoic glacial events and the rise of atmospheric oxygen: Earth and Planetary Science Letters, v. 225, p. 43–52.

Harder, H., 1976, Nontronite synthesis at low temperatures: Chemical Geology, v. 18, p. 169–180.

——1978, Synthesis of iron layer silicate minerals under natural conditions: Clays and Clay Minerals, v. 26, p. 65–72.

Hartlaub, R.P., Heaman, L.M., Chacko, T., and Ashton, K.E., 2007, Circa 2.3—Ga magmatism of the Arrowsmith orogeny, Uranium City region, western Churchill craton, Canada: Journal of Geology, v. 115, p. 181–195.

Haugaard, R., Frei, R., Stendal, H., and Konhauser, K., 2013, Petrology and geochemistry of the ~2.9 Ga Itilliarsuk banded iron formation and associated supracrustal rocks, West Greenland: Source characteristics and depositional environment: Precambrian Research, v. 229, p. 150–176.

Heimann, A., Johnson, C.M., Beard, B.L., Valley, J.W., Roden, E.E., Spicuzza, M.J., and Beukes, N.J., 2010, Fe, C, and O isotope compositions of banded iron formation carbonates demonstrate a major role for dissimilatory iron reduction in ~2.5 Ga marine environments: Earth and Planetary Science Letters, v. 294, p. 8–18.

Henderson, P., 1984, General geochemical properties and abundances of the rare earth elements, in Henderson, P., eds., Rare earth element geochemistry: Amsterdam, Elsevier, Developments in Geochemistry, p. 1–32.

Hou, K., Li, Y., Gao, J., Liu, F., and Qin, Y., 2014, Geochemistry and Si-O-Fe isotope constraints on the origin of banded iron formations of the Yuanjiacun Formation, Lvliang Group, Shanxi, China: Ore Geology Reviews, v. 57, p. 288–298.

Icopini, G.A., Anbar, A.D., Ruebush, S.S., Tien, M., and Brantley, S.L., 2004, Iron isotope fractionation during microbial reduction of iron: The importance of adsorption: Geology, v. 32, p. 205–208.

Isley, A.E., 1995, Hydrothermal plumes and the delivery of iron to banded iron formation: Journal of Geology, v. 103, p. 169–185.

Isley, A.E., and Abbott, D.H., 1999, Plume-related mafic volcanism and the deposition of banded iron formation: Journal of Geophysical Research, v. 104, p. 15461–15477.

Johnson, C.M., Beard, B.L., Beukes, N.J., Klein, C., and O'Leary, J.M., 2003, Ancient geochemical cycling in the Earth as inferred from Fe isotope studies of banded iron formations from the Transvaal craton: Contributions to Mineralogy and Petrology, v. 144, p. 523–547.

Johnson, C.M., Roden, E.E., Welch, S.A., and Beard, B.L., 2005, Experimental constraints on Fe isotope fractionation during magnetite and Fe carbonate formation coupled to dissimilatory hydrous ferric oxide reduction: Geochimica et Cosmochimica Acta, v. 69, p. 963–993.

Johnson, C.M., Beard, B.L., Klein, C., Beukes, N.J., and Roden, E.E., 2008, Iron isotopes constrain biologic and abiologic processes in banded iron formation genesis: Geochimica et Cosmochimica Acta, v. 72, p. 151–169.

Kamber, B.S., and Webb, G.E., 2001, The geochemistry of Late Archaean microbial carbonate: Implications for ocean chemistry and continental erosion history: Geochimica et Cosmochimica Acta, v. 65, p. 2509–2525.

Kappler, A., Pasquero, C., Konhauser, K.O., and Newman, D.K., 2005, Deposition of banded iron formation by anoxygenic phototrophic Fe(II)-oxidizing bacteria: Geology, v. 33, p. 865–868.

Karhu, J.A., and Holland, H.D., 1996, Carbon isotopes and the rise of atmospheric oxygen: Geology, v. 24, p. 867–870.

Kato, Y., Ohta, I., Tsunematsu, T., Watanabe, Y., Isozaki, Y., Maruyama, S., and Imai N., 1998, Rare earth element variations in mid-Archean banded iron formations: Implications for the chemistry of ocean and plate tectonics: Geochimica et Cosmochimica Acta, v. 62, p. 3475–3497.

Kaufman, A.J., 1996, Geochemical and mineralogic effects of contact metamorphism on banded iron-formation: An example from the Transvaal Basin, South Africa: Precambrian Research, v. 79, p. 171–194.

Kaufman, A.J., Hayes, J.M., and Klein, C., 1990, Primary and diagenetic controls of isotopic compositions of iron-formation carbonates: Geochimica et Cosmochimica Acta, v. 54, p. 3461–3473.

Klein, C., 2005, Some Precambrian banded iron-formations (BIFs) from around the world: Their age, geologic setting, mineralogy, metamorphism, geochemistry, and origin: American Mineralogist, v. 90, p. 1473–1499.

Klein, C., and Beukes, N.J., 1993, Proterozoic iron-formations, in Condie, K.C., eds., Proterozoic crustal evolution: Amsterdam, Elsevier, p. 383–418.

Köhler, I., Konhauser, K.O., Papineau, D., Bekker, A., and Kappler, A., 2013, Biological carbon precursor to diagenetic siderite with spherical structures in iron formations: Nature Communications, v. 4, p. 1741.

Konhauser, K.O., Hamade, T., Morris, R.C., Ferris, F.G., Southam, G., Raiswell, R., and Canfield, D., 2002, Could bacteria have formed the Precambrian banded iron formations?: Geology, v. 30, p. 1079–1082.

Konhauser, K.O., Newman, D.K., and Kappler, A., 2005, The potential significance of microbial Fe(III)-reduction during Precambrian banded iron formations: Geobiology, v. 3, p. 167–177.

Konhauser, K.O., Amskold, L., Lalonde, S.V., Posth, N.R., Kappler, A., and Anbar, A., 2007, Decoupling photochemical Fe(II) oxidation from shallow-water BIF deposition: Earth and Planetary Science Letters, v. 258, p. 87–100.

Konhauser, K.O., Lalonde, S.V., Planavsky, N., Pecoits, E., Lyons, T., Mojzsis, S., Rouxel, O.J., Barley, M., Rosiere, C., Fralick, P.W., Kump, L.R., and Bekker, A., 2011a, Chromium enrichment in iron formations record Earth's first acid rock drainage during the Great Oxidation Event: Nature, v. 478, p. 369–373.

Konhauser, K.O., Kappler, A.K., and Roden, E.E., 2011b, The microbial role in iron redox and biomineralization reactions: Elements, v. 7, p. 89–93.

Koziol, A.M., 2004, Experimental determination of siderite stability and application to Martian Meteorite ALH84001: American Mineralogist, v. 89, p. 294–300.

Krapež, B., Barley, M.E., and Pickard, A.L., 2003, Hydrothermal and resedimented origins of the precursor sediments to banded iron formation: Sedimentological evidence from the early Palaeoproterozoic Brockman Supersequence of Western Australia: Sedimentology, v. 50, p. 979–1011.

Kump, L.R., and Seyfried, W.E., 2005. Hydrothermal Fe fluxes during the Precambrian: Effect of low oceanic sulfate concentrations and low hydrostatic pressure on the composition of black smokers: Earth and Planetary Science Letters, v. 235, p. 654–662.

Laajoki, K., and Saikkonen, R., 1977, On the geology and geochemistry of the Precambrian iron formations, Väyrylänkylä, South Puolanka area, Finland: Geological Survey of Finland Bulletin 292, p. 1–137.

Li, Y.L., 2014, Micro-and nanobands in Late Archean and Palaeoproterozoic banded-iron formations as possible mineral records of annual and diurnal depositions: Earth and Planetary Science Letters, v. 391, p. 160–170.

Li, Y.L., Konhauser, K.O., Cole, D.R., and Phelps, T.J., 2011, Mineral ecophysiological data provide growing evidence for microbial activity in banded iron formations: Geology, v. 39, p. 707–710.

Li, Y.L., Konhauser, K.O., Kappler, A., and Hao, X.L., 2013, Experimental low-grade alteration of biogenic magnetite indicates microbial involvement in generation of banded iron formations: Earth and Planetary Science Letters, v. 361, p. 229–237.

Li, Z.H., Zhu, X.K., Tang, S.H., Li, J., and Liu, H., 2010, Characteristics of rare earth elements and geological significations of BIFs from Jidong, Wutai and Lüliang area: Geoscience, v. 24, p. 840–846 [in Chinese].

Liu, C.H., Zhao, G.C., Sun, M., Wu, F.Y., Yang, J.H., Yin, C.Q., and Leung, W.H., 2011, U-Pb and Hf isotopic study of detrital zircons from the Yejishan Group of the Lüliang Complex: Constraints on the timing of collision between the eastern and western blocks, North China craton: Sedimentary Geology, v. 236, p. 129–140.

Liu, C.H., Zhao, G.C., Liu, F.L., and Shi, J.R., 2014, Geochronological and geochemical constraints on the Lüliang Group in the Lüliang Complex: Implications for the tectonic evolution of the Trans-North China orogen: Lithos, v. 198, p. 298–315.

Liu, D.Y., Wilde, S.A., Wan, Y.S., Wu, J.S., Zhou, H.Y., Dong, C.Y., and Yin, X.Y., 2008, New U-Pb and Hf isotopic data confirm Anshan as the oldest preserved segment of the North China craton: American Journal of Science, v. 308, p. 200–231.

Liu, S.W., Zhang, J., Li, Q.G., Zhang, L.F., Wang, W., and Yang, P.T., 2012, Geochemistry and U-Pb zircon ages of metamorphic volcanic rocks of the Paleoproterozoic Lüliang Complex and constraints on the evolution of the Trans-North China orogen, North China craton: Precambrian Research, v. 222, p. 173–190.

Lovley, D.R., 1993, Dissimilatory metal reduction: Annual Reviews in Microbiology, v. 47, p. 263–290.

Master, S., 1991, Stratigraphy, tectonic setting, and mineralization of the Early Proterozoic Magondi Supergroup, Zimbabwe: A review: Johannesburg, University of Witwatersrand Economic Geology Research Unit, Information Circular 238, 75 p.

McCollom, T.M., 2003, Formation of meteorite hydrocarbons from thermal decomposition of siderite (FeCO$_3$): Geochimica et Cosmochimica Acta, v. 67, p. 311–317.

McLennan, S.M., 1989, Rare earth elements in sedimentary rocks: Influence of provenance and sedimentary processes: Reviews in Mineralogy and Geochemistry, v. 21, p. 169–200.

Miyano, T., and Beukes, N.J., 1984, Phase relations of stilpnomelane, ferriannite and riebeckite in very low-grade metamorphosed iron-formations: South African Journal of Geology, v. 87, p. 111–124.

Nealson, K.H., and Myers, C.R., 1990, Iron reduction by bacteria: A potential role in the genesis of banded iron formations: American Journal of Science, v. 290, p. 35–45.

Often, M., 1985, The Early Proterozoic Karasjok greenstone belt, Norway: A preliminary description of lithology, stratigraphy and mineralization: Norges Geologiske Undersøkelse Bulletin 403, p. 75–88.

Ohmoto, H., 2003, Nonredox transformations of magnetite-hematite in hydrothermal systems: ECONOMIC GEOLOGY, v. 98, p. 157–161.

Ohta, A., and Kawabe, I., 2001, REE(III) adsorption onto Mn dioxide (δ-MnO$_2$) and Fe oxyhydroxide: Ce(III) oxidation by δ-MnO$_2$: Geochimica et Cosmochimica Acta, v. 65, p. 695–703.

Paakola, J., 1971, The volcanic complex and associated manganiferous iron formation of the Porkonen-Pahtavaara area in Finnish Lapland: Bulletin de la Commission géologique de Finlande, v. 247, 82 p.

Partin, C.A., Bekker, A., Planavsky, N.J., Scott, C.T., Gill, B.C., Li, C., Podkovyrov, V., Maslov, A., Konhauser, K.O., Lalonde, S.V., Love, G.D., Poulton, S.W., and Lyons, T.W., 2013a, Large-scale fluctuations in Precambrian atmospheric and oceanic oxygen levels from the record of U in shales: Earth and Planetary Science Letters, v. 369–370, p. 284–293.

Partin, C.A., Lalonde, S.V., Planavsky, N.J., Bekker, A., Rouxel, O.J., Lyons, T.W., and Konhauser, K.O., 2013b, Uranium in iron formations and the rise of atmospheric oxygen: Chemical Geology, v. 362, p. 82–90.

Pecoits, E., Gingras, M.K., Barley, M.E., Kappler, A., Posth, N.R., and Konhauser, K.O., 2009, Petrography and geochemistry of the Dales Gorge banded iron formation: Paragenetic sequence, source and implications for palaeo-ocean chemistry: Precambrian Research, v. 172, p. 163–187.

Pickard, A.L., Barley, M.E., and Krapež, B., 2004, Deep-marine depositional setting of banded iron formation: Sedimentological evidence from interbedded clastic sedimentary rocks in the early Palaeoproterozoic Dales Gorge Member of Western Australia: Sedimentary Geology, v. 170, p. 37–62.

Planavsky, N., Rouxel, O., Bekker, A., Shapiro, R., Fralick, P., and Knudsen, A., 2009, Iron-oxidizing microbial ecosystems thrived in late Paleoproterozoic redox-stratified oceans: Earth and Planetary Science Letters, v. 286, p. 230–242.

Planavsky, N., Bekker, A., Rouxel, O.J., Kamber, B.S., Hofmann, A.W., Knudsen, A., and Lyons, T.W., 2010, Rare earth element and yttrium compositions of Archean and Paleoproterozoic Fe formations revisited: New perspectives on the significance and mechanisms of deposition: Geochimica et Cosmochimica Acta, v. 74, p. 6387–6405.

Planavsky, N., Rouxel, O.J., Bekker, A., Hofmann, A., Little C.T.S., and Lyon, T.W., 2012a, Iron isotope composition of some Archean and Proterozoic iron formations: Geochimica et Cosmochimica Acta, v. 80, p. 158–169.

Planavsky, N.J., Bekker, A., Hofmann, A., Owens, J.D., and Lyons, T.W., 2012b, Sulfur record of rising and falling marine oxygen and sulfate levels during the Lomagundi event: Proceedings of the National Academy of Sciences, v. 109, p. 18,300–18,305.

Posth, N.R., Hegler, F., Konhauser, K.O., and Kappler, A., 2008, Alternating Si and Fe deposition caused by temperature fluctuations in Precambrian oceans: Nature Geoscience, v. 1, p. 703–708.

Posth, N.R., Canfield, D.E., and Kappler, A., 2014, Biogenic Fe (III) minerals: From formation to diagenesis and preservation in the rock record: Earth-Science Reviews, v. 135, p. 103–121.

Rasmussen, B., Meier, D.B., Krapež, B., and Muhling, J.R., 2013a, Iron silicate microgranules as precursor sediments to 2.5-billion-year-old banded iron formations: Geology, v. 41, p. 435–438.

Rasmussen, B., Bekker, A., and Fletcher, I.R., 2013b, Correlation of Paleoproterozoic glaciations based on U-Pb zircon ages for tuff beds in the Transvaal and Huronian Supergroups: Earth and Planetary Science Letters, v. 382, p. 173–180.

Resende, M.G., and Jost, H., 1995, Petrogênese de formações ferríferas e metahidrotermalitos da formação aimbé, Grupo Guarinos (Arqueano), Goiás: Revista Brasileira de Geociencias, v. 25, p. 41–50.

Rouxel, O., Bekker, A., and Edwards, K., 2005, Iron isotope constraints on the Archean and Paleoproterozoic ocean redox state: Science, v. 307, p. 1087–1091.

Schidlowski, M., Eichmann, R., and Junge, C.E., 1976, Carbon isotope geochemistry of the Precambrian Lomagundi carbonate province, Rhodesia: Geochimica et Cosmochimica Acta, v. 40, p. 449–455.

Schröder, S., Bekker, A., Beukes, N.J., Strauss, H., and van Niekerk, H.S., 2008, Rise in seawater sulphate concentration associated with the Paleoproterozoic positive carbon isotope excursion: Evidence from sulphate evaporites in the 2.2–2.1 Gyr shallow-marine Lucknow Formation, South Africa: Terra Nova, v. 20, p. 108–117.

Schweigart, H., 1965, Genesis of the iron ores of the Pretoria series, South Africa: Economic Geology, v. 60, p. 269–298.

Schwertmann, U., and Murad, E., 1983, Effect of pH on the formation of goethite and hematite from ferrihydrite: Clays and Clay Minerals, v. 31, p. 277–284.

Scott, C., Wing, B.A., Bekker, A., Planavsky, N.J., Medvedev, P., Bates, S.M., Yun, M., and Lyons, T.W., 2014, Pyrite multiple-sulfur isotope evidence for rapid expansion and contraction of the early Paleoproterozoic seawater sulfate reservoir: Earth and Planetary Science Letters, v. 389, p. 95–104.

Shen, B.F., Song, L.S., and Li, H.Z., 1982, An analysis of the sedimentary facies and the formation condition of the Yuanjiacun iron formation, Lanxian County, Shanxi Province, China: Journal of Changchun Geological Institution, v. 25, p. 31–51 (in Chinese).

Shen, Q.H., 1998, The geological characteristics and forming geological background of the Early Precambrian banded itabirite in North China platform, in Cheng, Y.Q., eds., Precambrian geology study of North China platform: Beijing, Geological Publishing House, p. 1–30 (in Chinese).

Shen, Q.H., Song, H.X., and Zhao, Z.R., 2009, Characteristics of rare earth elements and trace elements in Hanwang Neo-Archaean banded iron formations, Shandong Province: Acta Geoscientica Sinica, v. 30, p. 693–699 (in Chinese).

Sholkovitz, E.R., Shaw, T., and Schneider, D.L., 1992, The geochemistry of rare earth elements in the seasonally anoxic water column and pore waters of Chesapeake Bay: Geochimica et Cosmochimica Acta, v. 56, p. 3389–3402.

Siever, R., 1992, The silica cycle in the Precambrian: Geochimica et Cosmochimica Acta, v. 56, p. 3265–3272.

Silver, P.G., and Behn, M.D., 2008, Intermittent plate tectonics?: Science, v. 319, p. 85–88.

Slack, J.F., Grenne, T., Bekker, A., Rouxel, O.J., and Lindberg, P.A., 2007, Suboxic deep seawater in the late Paleoproterozoic: Evidence from hematitic chert and iron formation related to seafloor-hydrothermal sulfide deposits, central Arizona, USA: Earth and Planetary Science Letters, v. 255, p. 243–256.

Smith, A.J., Beukes, N.J., and Gutzmer, J., 2013, The composition and depositional environments of Mesoarchean iron formations of the West Rand Group of the Witwatersrand Supergroup, South Africa: Economic Geology, v. 108, p. 111–134.

Tian, Y.Q., Yuan, G.P., Lu, J.R., Jing, Y., Yu, J.H., and Li, M.M., 1986, Research on formation conditions and tectonic characteristics of Precambrian Yuanjiacun metamorphic-sedimentary iron deposits in Lan County, Shanxi province: Shanxi, Geology and Mineral Resources Bureau Press, 270 p. (in Chinese).

Trendall, A.F., and Blockley, J.G., 1970, The iron-formations of the Precambrian Hamersley Group, Western Australia: Geological Survey of Western Australia Bulletin 119, 366 p.

Tsikos, H., and Moore, J.M., 1997, Petrography and geochemistry of the Paleoproterozoic Hotazel iron-formation, Kalahari manganese field, South Africa: Implications for Precambrian manganese metallogenesis: Economic Geology, v. 92, p. 87–97.

Wan, Y.S., Geng, Y.S., Shen, Q.H., and Zhang, R.X., 2000, Khondalite series-geochronology and geochemistry of the Jiehekou Group in Lüliang area, Shanxi Province: Acta Petrologica Sinica, v. 16, p. 49–58 (in Chinese).

Wan, Y.S., Dong, C.Y., Xie, H.Q., Wang, S.J., Song, M.C., Xu, Z.Y., Wang, S.Y., Zhou, H.Y., Ma, M.Z., and Liu, D.Y., 2012, Formation ages of Early Precambrian BIFs in the North China craton: SHRIMP zircon U-Pb dating: Acta Geologica Sinica, v. 86, p. 1447–1478 (in Chinese).

Wang, C.L., Zhang, L.C., Lan, C.Y., and Dai, Y.P., 2014, Rare earth element and yttrium compositions of the Paleoproterozoic Yuanjiacun BIF in the Lüliang area and their implications for the Great Oxidation Event (GOE): Science China Earth Sciences, v. 57, p. 2469–2485.

Wang, C.L., Zhang, L.C., Dai, Y.P., and Lan, C.Y., 2015, Geochronological and geochemical constraints on the origin of clastic meta-sedimentary rocks associated with the Yuanjiacun BIF from the Lüliang Complex, North China: Lithos, v. 212–215, p. 231–246.

Yao, P.H., 1993, Records of Chinese iron ore deposits: Beijing, Metallurgical Industry Press, 662 p. (in Chinese).

Yu, J.H., Wang, D.Z., and Wang, C.Y., 1997, Ages of the Lüliang Group and its main metamorphism in the Lüliang Mountains, Shanxi—evidence from single-grain zircon U-Pb ages: Geological Review, v. 43, p. 403–408 (in Chinese).

Zhai, M.G., and Santosh, M., 2013, Metallogeny of the North China craton: Link with secular changes in the evolving Earth: Gondwana Research, v. 24, p. 275–297.

Zhai, M.G., and Windley, B.F., 1990, The Archean and Early Proterozoic iron formation of North China: Their characteristics, geotectonic relations, chemistry and implications for crustal growth: Precambrian Research, v. 48, p. 267–286.

Zhang, L.C., Zhai, M.G., Zhang, X.J., Xiang, P., Dai, Y.P., Wang, C.L., and Pirajno, F., 2012a, Formation age and tectonic setting of the Shirengou Neoarchean banded iron deposit in eastern Hebei Province: Constraints from geochemistry and SIMS zircon U-Pb dating: Precambrian Research, v. 222, p. 325–338.

Zhang, L.C., Zhai, M.G., Wan, Y.S., Guo, J.H., Dai, Y.P., Wang, C.L., and Liu, L., 2012b, Study of the Precambrian BIF-iron deposits in the North China craton: Progresses and questions: Acta Petrologica Sinica, v. 28, p. 3431–3445 (in Chinese).

Zhang, X.J., Zhang, L.C., Xiang, P., Wan, B., and Pirajno, F., 2011, Zircon U-Pb age, Hf isotopes and geochemistry of Shuichang Algoma-type banded iron-formation, North China craton: Constraints on the ore-forming age and tectonic setting: Gondwana Research, v. 20, p. 137–148.

Zhao, G.C., and Zhai, M.G., 2013, Lithotectonic elements of Precambrian basement in the North China craton: Review and tectonic implications: Gondwana Research, v. 23, p. 1207–1240.

Zhao, G.C., Sun, M., Wilde, S.A., and Li, S.Z., 2005, Late Archean to Paleoproterozoic evolution of the North China craton: Key issues revisited: Precambrian Research, v. 136, p. 177–202.

Zhao, G.C., Wilde, S.A., Sun, M., Li, S.Z., Li, X.P., and Zhang, J., 2008, SHRIMP U-Pb zircon ages of granitoid rocks in the Lüliang Complex: Implications for the accretion and evolution of the Trans-North China orogen: Precambrian Research, v. 160, p. 213–226.

Zhu, J.C., and Zhang, F.S., 1987, The formation condition of the Precambrian iron ores in Yuanjiacun ore deposit, Shanxi Province: Mineralium Deposita, v. 6, p. 11–21 (in Chinese).

Zhu, J.C., Zhang, F.S., and Xu, K.Q., 1988, Depositional environment and metamorphism of Early Proterozoic iron formation in the Lüliangshan region, Shanxi Province, China: Precambrian Research, v. 39, p. 39–50.